Supporting Information

Precision Molecular Threading/Dethreading

Jessica Groppi[+], Lorenzo Casimiro[+], Martina Canton, Stefano Corra, Mina Jafari-Nasab, Gloria Tabacchi, Luigi Cavallo, Massimo Baroncini, Serena Silvi, Ettore Fois,* and Alberto Credi*

anie_202003064_sm_miscellaneous_information.pdf
anie_202003064_sm_Movie_S1.mp4
anie_202003064_sm_Movie_S2.mp4
anie_202003064_sm_Movie_S3.mp4
anie_202003064_sm_Movie_S4.mp4

Contents

1. Materials and experimental methods

General materials

Dibenzylammonium Hexafluorophosphate ($\mathbf{1}^+$) was prepared according to literature procedures.[1] All reagents and chemicals were purchased from Sigma-Aldrich or VWR international and used as received unless otherwise stated. Solvents were dried according to literature procedures. Flash column chromatography was performed using Sigma Aldrich Silica 40 (230-400 mesh size or 40-63 mm) as the stationary phase. Thin layer chromatography was performed on TLC Silica gel 60 F254 coated aluminum plates from Merck.

Experimental methods

NMR spectra were recorded on an Agilent DD2 spectrometer operating at 500 MHz. Chemical shifts are quoted in ppm relative to tetramethylsilane using the residual solvent peak as a reference standard and all coupling constants (J) are expressed in Hertz (Hz).

UV-Visible absorption spectra were recorded with Agilent Technologies Cary 300 spectrophotometers. The measurements were performed at room temperature (298 ± 2 K) on air-equilibrated CH_2Cl_2 (Merck Uvasol) solutions contained in quartz cuvettes (optical path length = 1.0 cm). The comparison of the absorption spectrum of mixed solutions with the sum of the spectra of the same solutions before mixing was performed using a dedicated 1-cm tandem spectrophotometric cell with two compartments separated by a quartz wall with an aperture that allows manual mixing (total optical path length = 0.9 cm).

Spectrophotometric titrations were performed by adding small (5-10 μL) aliquots a concentrated solution of the ammonium guest to a more dilute solution of the DB24C8 host. The thermodynamic binding constants were obtained by fitting the absorbance-concentration curves at selected wavelengths with the software SPECFIT[2] according to a 1:1 binding model.

Reaction kinetic profiles were collected on air-equilibrated CH_2Cl_2 (Romil) solutions at 298 ± 2 K in the spectrophotometer, by monitoring the absorption changes as a function of time after mixing equimolar solutions of the two components in the above described tandem cuvette. Alternatively, experiments were performed by adding a concentrated solution of one component to a more dilute solution of the other, in order to obtain the desired stoichiometric ratio. In the case of compound $\mathbf{1}^+$, which exhibits a very fast threading into DB24C8, kinetics was investigated by means of a stopped flow spectrometer (Applied Photophysics SX 18-MV). The standard flow tube used had an

observation path length of 1.0 cm, and the driving ram for the mixing system was operated at the recommended pressure of 8.5 bar. Under these conditions, the dead time (i.e., the time required to fill the cell) was about 2 ms, as determined with a test reaction. In all cases the experimental data were fitted with the software SPECFIT[2] using a mixed order reaction (second order for threading, first order for dethreading), with the constrain that the ratio between the two rate constants has to be equal to the thermodynamic constant determined from titrations.

The lower- and upper-limiting values of the threading rate constants (k_{in}) for the fastest and slowest processes, respectively, were evaluated with a conservative estimate.

Fastest process. For the threading reaction (second order process)

$$k_{in} = \frac{1}{t_{\frac{1}{2}} \times c_0} \tag{S1}$$

where $t_{\frac{1}{2}}$ is the half life of the reaction and c_0 is the initial concentration of the components (mixed in equimolar amount). As no signal change was observed in stopped flow experiments, it can be safely assumed that the reaction is over within the dead time of the technique (2 ms, vide supra) – that is, $t_{\frac{1}{2}} < 2$ ms. Since the lowest concentration value employed in the experiment was $c_0 = 2.5 \times 10^{-5}$ M, the application of equation S1 yields a lower-limiting value for k_{in} of 2×10^7 L mol^{-1} s^{-1}.

Slowest processes. In the case of the slowest processes, a 1:1 mixture of the axle and ring components ($c_0 = 5.0 \times 10^{-3}$ M) was let to equilibrate at room temperature and monitored by ^{1}H NMR. In all cases, no sign of complex formation was detected after 72 h. The upper-limiting value for k_{in} was calculated with equation S2, derived from a second-order rate equation

$$k_{in} = \left(\frac{1}{c_t} - \frac{1}{c_0} \right) / t \tag{S2}$$

Under the safe assumption of a detection limit of 5% for the complex by NMR spectroscopy, the concentration of the complex at $t = 72$ h (259200 s) must be lower than 2.5×10^{-4} M; this implies that the concentration of the free components, c_t, is at least 4.75×10^{-3} M. Inserting these numbers in equation S2 yields an upper-limiting value for k_{in} of 7×10^{-5} L mol^{-1} s^{-1}.

Synthetic procedures

**General procedure for the synthesis of the symmetric salts**

The symmetric secondary amines were obtained following a synthetic approach adapted from literature procedures.[3] The procedure consisted in mixing the aldehyde (2 mmol) with hexamethyldisilazane (HMDS) (4 mmol), followed by the addition of $LiClO_4$ (2 mmol). The reaction mixture was stirred for 1 hour at 60°C. After cooling at 0°C, the reaction mixture was dissolved in dry MeOH (20 ml) and $NaBH_4$ (6 mmol) was added portion wise. The reaction mixture was allowed to warm up to room temperature and it was left stirring until the control TLC showed the complete consumption of the starting aldehyde (typically 3-4 hours). The solvent was removed under vacuum and the reaction crude was dissolved in saturated $NaHCO_3$ (aq) (50 ml) and the crude product was extracted with ethyl acetate (150 ml). The organic phase was dried over Na_2SO_4 and the solvent removed to obtain a colorless oil. In order to obtain the secondary ammonium salts, the reaction crude was dissolved in CH_3CN and a few drops of HCl (36%) were added to precipitate the chloride salts. The hexafluorophosphate salts were obtained from the chlorides by anion exchange. The chloride salts were dissolved in the minimum volume of H_2O or acetone and a large excess of NH_4PF_6 was added to precipitate the hexafluorophosphate salts.
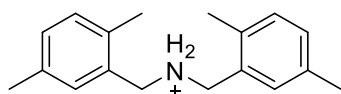
Bis(3,5-dimethylbenzyl)ammonium hexafluorophosphate (2$^+$)
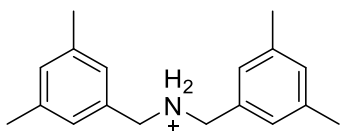
The product was a white solid obtained in 50 % yield. **¹H-NMR (500 MHz, CD₃CN, 298 K):** *δ (ppm)* 7.26 (t, *J* = 7.6, 2H, ArH), 7.14 (d, *J* = 7.6, 4H, ArH), 6.70 (bs, 2H, NH₂) 4.30 (t, *J* = 6.3, 4H, CH₂), 2.37 (s, 12H, CH₃). **¹³C-NMR (125 MHz, CD₃CN, 298 K):** *δ (ppm)* 139.9, 132.1, 131.1, 128.7, 52.3, 21.2. **¹⁹F-NMR (470 MHz, CD₃CN, 298 K):** *δ (ppm)* −72.8 (d, *J_{F-P}* = 706 Hz).

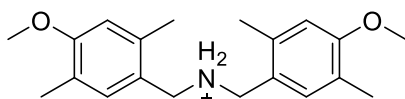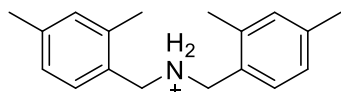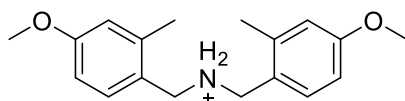**Bis(2,6-dimethylbenzyl)ammonium hexafluorophosphate (3$^+$)**
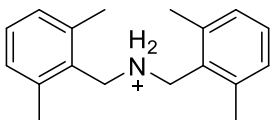
The product was a white solid obtained in 20 % yield. **¹H-NMR (500 MHz, CD₃CN, 298 K):** *δ (ppm)* 7.11 (s, 2H, ArH), 7.05 (s, 4H, ArH), 6.95 (bs, 2H, NH₂) 4.12 (s, 4H, CH₂), 2.32 (s, 12H, CH₃). **¹³C-NMR (125 MHz, CD₃CN, 298 K):** *δ (ppm)* 139.7, 131.1, 129.9, 128.2, 47.27, 20.1. **¹⁹F-NMR (470 MHz, CD₃CN, 298 K):** *δ (ppm)* −72.8 (d, *J_{F-P}* = 706 Hz).

Bis(2,5-dimethylbenzyl)ammonium hexafluorophosphate (4$^+$)

The product was a white solid obtained in 67 % yield. **^{1}H-NMR (500 MHz, CD$_3$CN, 298 K):** δ (ppm) 7.22 (s, 2H, ArH), 7.18 (s, 4H, ArH), 6.94 (bs, 2H, NH$_2$) 4.17 (t, J = 6.1, 4H, CH$_2$), 3.82 (s, 6H, OCH$_3$), 2.29 (s, 6H, CH$_3$), 2.15 (s, 6H, CH$_3$). **^{13}C-NMR (125 MHz, CD$_3$CN, 298 K):** δ (ppm) 137.3, 135.6, 132.0, 131.9, 131.5, 129.6, 49.7, 20.8, 18.8. **^{19}F-NMR (470 MHz, CD$_3$CN, 298 K):** δ (ppm) −72.8 (d, $J_{F\text{-}P}$ = 706 Hz).

Bis(4-methoxy-2,5-dimethylbenzyl)ammonium hexafluorophosphate (5$^+$)

The product was a white solid obtained in 20 % yield. **^{1}H-NMR (500 MHz, CD$_3$CN, 298 K):** δ (ppm) 7.15 (s, 2H, ArH), 6.81 (s, 2H, ArH), 6.78 (bs, 2H, NH$_2$) 4.12 (s, 4H, CH$_2$), 2.32 (s, 12H, CH$_3$). **^{13}C-NMR (125 MHz, CD$_3$CN, 298 K):** δ (ppm) 159.6, 138.0, 133.9, 125.4, 121.1, 113.5, 56.2, 49.2, 19.3, 15.8. **^{19}F-NMR (470 MHz, CD$_3$CN, 298 K):** δ (ppm) −72.8 (d, $J_{F\text{-}P}$ = 706 Hz).

Bis(2,4-dimethylbenzyl)ammonium hexafluorophosphate (6$^+$)

The product was a white solid obtained in 60 % yield. **^{1}H-NMR (500 MHz, CD$_3$CN, 298 K):** δ (ppm) 7.28 (d, J = 7.7, 2H, ArH), 7.11 (m, 4H, ArH), 4.25 (s, 4H, CH$_2$), 2.32 (s, 6H, CH$_3$), 2.29 (s, 6H, CH$_3$) **^{13}C-NMR (125 MHz, CD$_3$CN, 298 K):** δ (ppm) 141.1, 138.7, 132.7, 131.6, 128.2, 126.9, 49.5, 21.2, 19.3 **^{19}F-NMR (470 MHz, CD$_3$CN, 298 K):** δ (ppm) −72.8 (d, $J_{F\text{-}P}$ = 706 Hz).
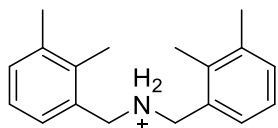
Bis(4-methoxy-2-methylbenzyl)ammonium hexafluorophosphate (7$^+$)

The product was a white solid obtained in 30 % yield. **^{1}H-NMR (500 MHz, CD$_3$CN, 298 K):** δ (ppm) 7.33 (d, J = 8.3, 2H, ArH), 6.84 (m, 4H, ArH), 6.77 (bs, 2H, NH$_2$), 4.22

(s, 4H, CH$_2$), 3.79 (s, 6H, OCH$_3$), 2.31 (s, 6H, CH$_3$) **^{13}C-NMR (125 MHz, CD$_3$CN, 298 K):** δ *(ppm)* 161.7, 140.7, 133.4, 121.8, 117.3, 112.8, 56.0, 49.2, 19.6 **^{19}F-NMR (470 MHz, CD$_3$CN, 298 K):** δ *(ppm)* –72.8 (d, J_{F-P} = 706 Hz).

Bis(2,3-dimethylbenzyl)ammonium hexafluorophosphate (8$^+$)

The product was a white solid obtained in 55 % yield. **^{1}H-NMR (500 MHz, CD$_3$CN, 298 K):** δ *(ppm)* 7.26 (m, 4H, ArH), 7.18 (t, J = 7.6, 2H, ArH), 6.93 (bs, 2H, NH$_2$), 4.32 (t, J = 7.6, 4H, CH$_2$), 2.31 (s, 6H, CH$_3$), 2.22 (s, 6H, CH$_3$). **^{13}C-NMR (125 MHz, CD$_3$CN, 298 K):** δ *(ppm)* 139.2, 137.38, 132.4, 129.6, 127.1, 50.3, 20.7, 15.7. **^{19}F-NMR (470 MHz, CD$_3$CN, 298 K):** δ *(ppm)* –72.8 (d, J_{F-P} = 706 Hz).

Bis(3,4-dimethylbenzyl)ammonium hexafluorophosphate (9$^+$)
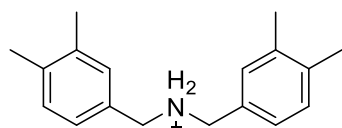
The product was a white solid obtained in 20 % yield. **^{1}H-NMR (500 MHz, CD$_3$CN, 298 K):** δ *(ppm)* 7.21 (m, 4H, ArH), 7.17 (m, 2H, ArH), 6.97 (bs, 2H, NH$_2$), 4.13 (t, J = 6.2, 4H, CH$_2$), 2.28 (s, 12H, CH$_3$) **^{13}C-NMR (125 MHz, CD$_3$CN, 298 K):** δ *(ppm)* 139.5, 138.5, 132.2, 131.1, 128.7, 128.6, 52.2, 19.8, 19.6. **^{19}F-NMR (470 MHz, CD$_3$CN, 298 K):** δ *(ppm)* –72.8 (d, J_{F-P} = 706 Hz).

Bis(4-methoxy-3-methylbenzyl)ammonium hexafluorophosphate (10$^+$)
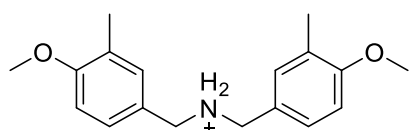
The product was a white solid obtained in 35 % yield. **^{1}H-NMR (500 MHz, CD$_3$CN, 298 K):** δ *(ppm)* 7.26 (d, J = 8.3, 2H, ArH), 7.21 (s, 2H, ArH), 6.94 (d, J = 8.3, 2H, ArH), 6.87 (bs, 2H, NH$_2$), 4.10 (t, J = 6.2, 4H, CH$_2$), 3.83 (s, 6H, OCH$_3$), 2.19 (s, 6H, CH$_3$) **^{13}C-NMR (125 MHz, CD$_3$CN, 298 K):** δ *(ppm)* 159.8, 133.4, 130.3, 128.0, 122.8, 118.3, 111.4, 56.2, 51.8, 16.3. **^{19}F-NMR (470 MHz, CD$_3$CN, 298 K):** δ *(ppm)* –72.8 (d, J_{F-P} = 706 Hz).

2. Computational details

Quantum chemical calculations in the gas phase

The structure of the complexes of dibenzo[24]crown-8 (DB24C8) with the ammonium-type guests **6**[+] and **8**[+] and of their respective constituent parts were optimized by adopting a gaussian basis set, and the range-separated hybrid functional ωB97XD[4] as density functional approximation to DFT.

The binding energies of the adducts [BE(complex)] were obtained from the difference between the total energy of the complex E(complex) and the sum of the energies of the minimum energy structures of the separated ring and axle components [E(DB24C8) and E(guest), respectively], according to the following equation:

$$BE(complex) = E(complex) - E(DB24C8) - E(guest) \qquad (S3)$$

With this definition, a negative value of the binding energy of a complex indicates an energy gain in the formation of the complex *i.e.*, the complex is more stable than the sum of the separated components, and its formation is thermodynamically favoured.

Within the same quantum-chemical framework, the harmonic frequencies and the vibrational eigenmodes of the [**6**⊂DB24C8][+]/[**8**⊂DB24C8][+] complexes and of their isolated components were computed at the same level of theory. The energy minima had all positive frequencies. The zero-point-energy (ZPE) of each species was calculated using the unscaled harmonic frequencies; these quantities were used to obtain the final ZPE-corrected binding energies of the supramolecular complexes.

All these quantum chemical calculations, including the below-described transition state optimization and thermochemistry, were performed with the Gaussian 09 code[5] and by adopting the full double ζ plus polarization D95(d,p) basis set.

In the case of the [**6**⊂DB24C8][+] system, a transition state search has been performed using as educated guess the geometry of the highest energy configuration sampled along the metadynamics simulation of the [**6**⊂DB24C8][+] dethreading process (for the computational details of the plane-wave calculations and metadynamics simulation, see next paragraph). The geometry of the transition state for the dethreading has been optimized at the PBE-D2/D95(d,p) level of theory – *i.e.,* using the same density functional approximation adopted in the metadynamics finite temperature simulation and in the transition state search with plane waves basis set (namely PBE-D2, *vide infra*). Also the structure of the threaded [**6**⊂DB24C8][+] was re-optimized at the PBE-D2/ D95(d,p) level of theory in order to calculate the energetics and thermochemistry of the transition state. The thermochemical properties of the transition state have been

calculated at 298 K. In addition, the transition-state optimization and the calculation of its thermochemical properties were also performed by adopting the above-mentioned range-separated hybrid functional ωB97xd and the same D95(d,p) basis set. In both PBE-D2 and ωB97xd cases, a vibrational analysis was performed on the optimized geometry of the transition state, yielding exactly one normal mode with an imaginary frequency (one negative eigenvalue). Zero point energy and all frequency-related quantities were calculated from the unscaled harmonic frequencies.

For both the adopted DFT functionals, the solvation effects on the thermochemical properties of the transition state have been taken into account by using an implicit solvent model on both the $[6\subset DB24C8]^+$ minimum energy structure and the transition state for the dethreading. The solvation energies were calculated with the polarizable continuum model (PCM) using the dichloromethane parameters for the solvent.[6]

Ab-initio molecular dynamics and metadynamics simulations

To investigate the dethreading processes of symmetric dibenzylammonium ions with DB24C8, we selected two representative complexes, $[6\subset DB24C8]^+$ and $[8\subset DB24C8]^+$, which, according to the experimental results, showed opposite "yes"-"no" behavior in the dethreading experiments (namely, $[6\subset DB24C8]^+$ = "threading"; $[8\subset DB24C8]^+$ = "non-threading"). For these two systems, the dethreading process was modelled via *ab initio* molecular dynamics[7] enriched by statistical sampling. In particular, we adopted the *ab initio* metadynamics[8] methodology.

For these calculations, a Generalized Gradient Approximation to density functional theory (DFT) was used to describe electron-electron interactions – namely, the widely adopted PBE functional along with empirical dispersion corrections (*i.e.* PBE-D2).[9,10] Ion cores-electron interactions were modelled with ultra-soft pseudopotentials.[11] We used plane-waves (PW) as basis set. The cutoffs for the PW expansion of wavefunctions and density were 25 Ry and 200 Ry respectively. Calculations were carried out with periodic boundary conditions, which were applied to a simulation cubic cell of size 22.55×22.55×22.55 Å, sufficient to perform a Γ-point-only k-point sampling, as well as to minimize interactions of the complex with its periodic images.

Each simulation system was constituted by the neutral ring DB24C8 and by the positively charged axle (6^+ or 8^+). The PF_6^- counter-ion was included in the model, as well as 96 CH_2Cl_2 molecules. In both cases, the simulation cell contained a total of 594 atoms.

For both model systems, *ab initio* molecular dynamics (AIMD) equilibration simulations (elapsed time: 10 ps) were performed at 300K (27°C), corresponding to the upper bound

of the conditions in which the experiments were conducted (T=25 ± 2 °C). This temperature was chosen in order to favour a faster equilibration of the system. The simulations were performed in the NVT ensemble, by applying Nose-Hoover chain thermostats to the ionic degrees of freedom.[12,13] The AIMD equations of motion[7,14] were integrated with a time step of 5 atomic units (a.u.) corresponding to 0.121 fs. The (fictitious) mass of the wavefunction's coefficients was 500 a.u.

The dethreading process was investigated by performing *ab initio* metadynamics. For both model systems, we selected as collective variable (CV) the displacement of all the 9 carbon atoms of one phenyl ring of the axle (including the C atoms of its methyl and methylene substituents) with respect to the 8 oxygen atoms of the macrocycle. For the evolution of the CV, we employed the Lagrange-Langevin dynamics with friction of 0.001 a.u. The selected target temperature was 300 K as in the equilibration runs. The metadynamics parameters adopted for the gaussian hills in the production simulations were the following for both systems: perpendicular width = 0.02 a.u., height = 0.002 a.u. By employing this computational protocol, a nearly complete dethreading of axle 6^+ from the DB24C8 ring was accomplished in ~2400 metadynamics steps, corresponding to about 350000 AIMD steps (42.1 ps total elapsed time). On the contrary, no dethreading of the axle 8^+ from the DB24C8 ring was achieved in a total of 1200 metadynamics steps – corresponding to about 175000 AIMD steps (21.2 ps total elapsed time). Such a metadynamics simulation was terminated because the free energy barrier had already reached a value above 100 kcal/mol.

In the case of the complex formed by the axle 10^+ with the DB24C8 ring, the dethreading process was simulated by performing the metadynamics simulation in the gas phase. The parameters adopted in this metadynamics run were the same as in the metadynamics simulations performed with the solvent molecules and the counterions.

All PW calculations were carried out with the CPMD (Car-Parrinello-Molecular-Dynamics) computer program[15] running on the Shaheen II supercomputer at Kaust.

The very long time scale of the reorganization of solvent molecules as a consequence of the displacement of the axle from the macrocycle, related to the Brownian motion, makes it very difficult to reach a truly equilibrated configuration of the separated DB24C8 and 6^+ components after the dethreading of the complex. For this very reason, the minimum energy structure of the separate components in solution – and hence the binding energy of the supramolecular complex in solution – cannot be accurately reproduced by our *ab initio* simulations. Nonetheless, although it is not possible to evaluate the binding energy of the complex at the process conditions and to compare it with the experimental $\Delta G°$, the free energy barrier for dethreading can be estimated

(with an uncertainty within about 5 kcal/mol) and directly compared with the experimental $\Delta G^{\ddagger}_{out}$ (see Table 2 in the main text, and Table S2).

To estimate the effect of the explicit solvent and its thermal behavior, a transition state search via geometry optimization was performed for the dethreading of $[6 \subset DB24C8]^+$ without the solvent molecules and using the partitioned rational function optimizer (P-RFO) implemented in the CPMD code.[16] The convergence criterion was 10^{-5} a.u. for the maximum force on nuclei.

3. Supplementary computational results

Binding energies of the gas phase supramolecular complexes

Prior to the study of the dethreading process, we investigated the energetics of two members of the class of the ten ammonium axles considered in this work, in order to establish whether the threaded complexes were thermodynamically stable in the gas phase and to identify the intermolecular interactions responsible of the stability of the (pseudo)rotaxanes. The selected guests are those denoted as 6^+ and 8^+ in Scheme 1 of the main text.

The minimum energy structures of the supramolecular complexes of 6^+ and 8^+ with DB24C8, indicated as $[6 \subset DB24C8]^+$ and $[8 \subset DB24C8]^+$, respectively, are graphically represented in Figure 2 of the main text. The hydrogen-bonding of both NH_2^+ protons of 6^+ and 8^+ with oxygen atoms of the macrocycle is shown in detail in Figure S1.

The zero point energy (ZPE) corrected binding energies calculated for the minimum structures of the $[6 \subset DB24C8]^+$ and $[8 \subset DB24C8]^+$ adducts were -73.33 and -73.32 kcal/mol, respectively (see Table S1). The high values of the binding energy indicate that both complexes are much more stable than the sum of their isolated constituents, hence their formation would be thermodynamically favored. The very close binding energies of the two compounds suggest a comparable stabilization of these complexes with respect to their isolated ring and axle components.

Besides electrostatic and Van der Waals interactions, which are ubiquitous in this kind of complexes, the main interactions responsible of the stabilization of the compounds are hydrogen bonds formed by both the NH_2^+ protons of the axle with oxygen atoms of the macrocycle, and π-π stacking interactions. The [N–H···O] distances, very similar between the two complexes (see Figure S1), indicate a significant hydrogen bonding interaction. The rather long distances between the guests' CH_2 protons from the closest oxygen atoms of the ring (around 2.4 Å for both complexes, see Figure S1) indicate that

the [C–H···O] interactions are weak and should play a less significant role than both [N–H···O] hydrogen bonding and π-π stacking.
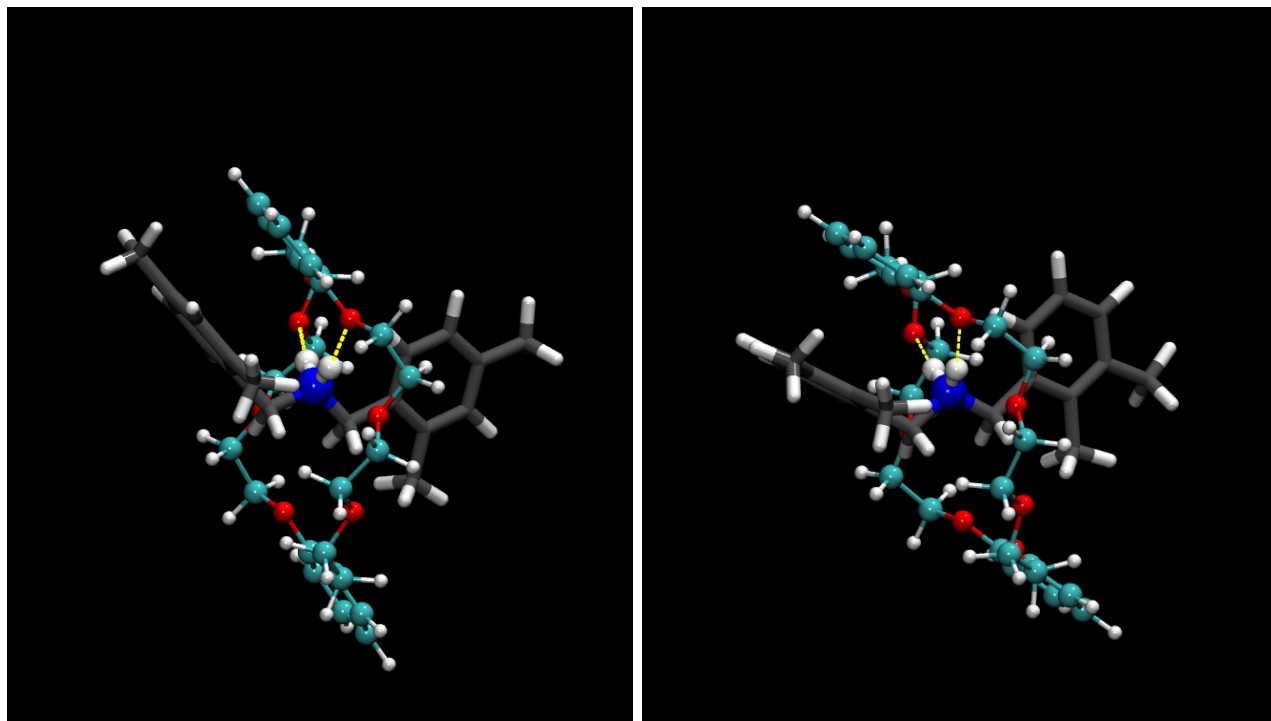

Figure S1. Ball and stick representation of the minimum energy structures of the complexes of DB24C8 with: **6**[+] (left panel) and **8**[+] (right panel), highlighting the two hydrogen bonds (HB) formed by the -NH$_2$ group of the axle with two oxygens of the macrocycle (yellow dashed lines). The hydrogen bonding distances are: 1.914 Å and 2.066 Å for **6**[+]; 1.893 Å and 2.063 Å for **8**[+]. The distances of the CH$_2$ groups of the axle from the closest DB24C8 oxygens are: 2.472 Å and 2.490 Å for **6**[+], 2.390 Å and 2.489 Å for **8**[+]. These distances suggest a weak [C–H···O] interaction. Color codes: C (ring) = cyan; C (axle) = grey; O = red; N = blue, H = white.

Energies (kcal/mol)	[6⊂**DB24C8**]$^+$	[8⊂**DB24C8**]$^+$
BE	−77.54	−76.98
BE (with ZPE)	−73.33	−73.32

Table S1. Binding energies BE (also including ZPE-corrections) calculated for the gas-phase minimum energy structures of the [**6**⊂DB24C8]$^+$ and [**8**⊂DB24C8]$^+$ complexes.

To estimate the stabilizing effect of the π-π stacking interactions, we optimized the geometry of an alternative conformation of the [**6**⊂DB24C8]$^+$ adduct, which featured a limited degree of π-π stacking between the axle and the ring. This alternative conformation (BE = −72.31 kcal/mol) has a smaller binding energy than the

[$6\subset$DB24C8]$^+$ energy minimum (BE = –77.54 kcal/mol): the energy difference amounts to 5.23 kcal/mol. By considering the close structural similarity of guests $\mathbf{1}^+$-$\mathbf{10}^+$, we may estimate that the presence of π-π stacking would impart a stabilization of about 5 kcal/mol to the supramolecular complexes of DB24C8 with the ammonium axles considered in this work.

Finally, to estimate the effect of the reciprocal orientation of the two phenyl moieties, we also optimized a conformation of [$6\subset$DB24C8]$^+$ in which one of the phenyl group was rotated by 180° around the C-CH$_2$ axis. This resulted in another optimized structure only slightly higher in energy (ΔE = +1.2 kcal/mol) with respect to the minimum energy structure depicted in Figure S1 (left panel). This calculation indicates that the reciprocal orientation of the two phenyl groups of the axle should not significantly affect the energetics of the (de)threading process.

Transition state geometry and thermochemistry from static quantum-chemical calculations

The transition state search relative to [$6\subset$DB24C8]$^+$ dethreading, performed with static QM calculations (0 K optimization of the transition state geometry) using the PBE-D2 and ωB97xd functionals with the D95(d,p) basis set, resulted in two optimized transition state structures – indicated as TS-PBE-D2 and TS-ωB97xd, respectively – each characterized by exactly one normal mode with negative eigenvalue. As reported in Table S2, the activation free energies for dethreading $\Delta G^{\ddagger}_{out}$ calculated with these functionals (inclusive of the solvation energy with implicit CH$_2$Cl$_2$ solvent) are very similar between each other, and appreciably higher than both the metadynamics and experimental values (see main text for discussion).

For a deeper insight on the effects of the explicit treatment of the solvent thermal motion, the difference of electronic energy ΔE_{el} calculated (at 0 K) for the transition state with respect to the threaded complex at the PBE-D2/D95(d,p) and ωB97xd/D95(d,p) levels is compared in Table S2 with the same quantity computed with PBE-D2 and plane wave basis sets. It is apparent that, independently on the level of theory, the ΔE_{el} values are all well above 30 kcal/mol, while the Δzpe, although dependent on the adopted level of theory – is much smaller in comparison. As a result, the zpe-corrected energy differences between the transition state and the minimum structure of [$6\subset$DB24C8]$^+$ calculated at the ωB97xd/D95(d,p), PBE-D2/D95(d,p), and PBE-D2/pw levels are all above 30 kcal/mol as well (see $\Delta E_{el,zpe}$ in Table S2). This picture does not change if solvation energy differences ΔE_{sol} calculated for the ωB97xd/D95(d,p) and PBE-D2/D95(d,p) cases are also considered (see $\Delta E_{el,zpe,sol}$ in Table S2). Indeed, the solvation energy differences ΔE_{sol} between the transition state and

the threaded complex, calculated with implicit solvent, are both in favor of the transition state, yet they are much smaller than the electronic energy differences ΔE_{el}.

Energies (kcal/mol)	ωB97xd	PBE-D2	PBE-D2/pw	PBE-D2/MTD	Exp
ΔE_{el}	37.7	34.3	32.4	-	-
Δzpe	−1.7	−0.6	−0.3	-	-
$\Delta E_{el,zpe}$	36.0	33.7	32.1	-	-
ΔE_{sol}	−2.2	−1.6	-	-	-
$\Delta E_{el,zpe,sol}$	33.8	32.1	-	-	-
$\Delta G^{\ddagger}_{out,\ no\ solvent}$	35.2	36.0	-	-	-
$\Delta G^{\ddagger}_{out}$	33.0	34.4	-	19.8	23.1

Table S2. Differences of electronic energy ΔE_{el}, zero-point energy Δzpe, zpe-corrected electronic energy ΔE_{zpe}, solvation energy ΔE_{sol}, and solvent-corrected-zpe-corrected electronic energy $\Delta E_{el,zpe,sol}$ for the transition state with respect to the minimum structure of threaded [**6**⊂DB24C8][+]. Activation free energies with implicit solvent $\Delta G^{\ddagger}_{out}$ and without implicit solvent $\Delta G^{\ddagger}_{out,\ no\ solvent}$ from static quantum chemical calculations at the PBE-D2/D95(d,p) and ωb97xd/D95(d,p) levels. ΔE_{el}, Δzpe, and $\Delta E_{el,zpe}$ values from static calculations with plane waves basis set (PBE-D2/pw), and $\Delta G^{\ddagger}_{out}$ values from metadynamics (PBE-D2/MTD) and experiment (Exp) are included for comparison.

As a consequence, the activation free energies for dethreading calculated without implicit solvent ($\Delta G^{\ddagger}_{out,\ no\ solvent}$) are very close to $\Delta G^{\ddagger}_{out}$, and of the same order of ΔE_{el}. These results indicate that the main contribution to the $\Delta G^{\ddagger}_{out}$ values at the PBE-D2/D95(d,p) and ωB97xd/D95(d,p) levels is mostly constituted by electronic energy. The significantly lower $\Delta G^{\ddagger}_{out}$ value obtained from metadynamics suggests therefore that the thermal motion of the solvent molecules plays indeed a leading role in lowering the activation barrier for the dethreading of the rotaxane, as also discussed in the main text.

The characteristic negative-eigenvalue normal mode for the transition state optimized with the ωB97xd functional is illustrated in Movie S4 (the negative-eigenvalue mode obtained for PBE-D2/D95(d,p) and PBE-D2/pw are nearly identical to the ωB97xd case). In all three cases, the vibrational mode of the transition state is characterized by the relative atomic displacements of the slipping phenyl group of the axle, with respect to the DB24C8 ring. Significantly, such a mode nicely reproduces the collective variable selected for the metadynamics simulation – the displacement of the C atoms of the phenyl group with respect to the O atoms of the ring.

A closer inspection of the geometrical parameters of the transition state underlines the strict similarity of the three transition state structures obtained with static calculations –

i.e., TS-ωB97xd, TS-PBE-D2/D95(d,p) and TS-PBE-D2/pw (Table S3). Interestingly, while in the corresponding minimum structures (GS-ωB97xd, GS-PBE-D2/D95(d,p) and GS-PBE-D2/pw, respectively) a $-NH_2^+-$ proton was hydrogen bonded to two DB24C8 oxygens (O1 and O2'), all the three transition states exhibit a single, but significantly stronger, hydrogen bond. Also importantly, a change of ellipticity of the ring takes place in passing from the fully threaded complex to the transition state, as evidenced by the variation of the oxygen-oxygen distances (Table S3). Such a peculiar deformation undergone by the DB24C8 ring in the transition state with respect to the threaded rotaxanes is illustrated in Scheme S1. Notably, the static calculations performed with all the three approaches reproduce such an elliptical-to-circular structural change, also manifested by the activated complex in the metadynamics simulation.

GS-ωB97xd   TS-ωB97xd
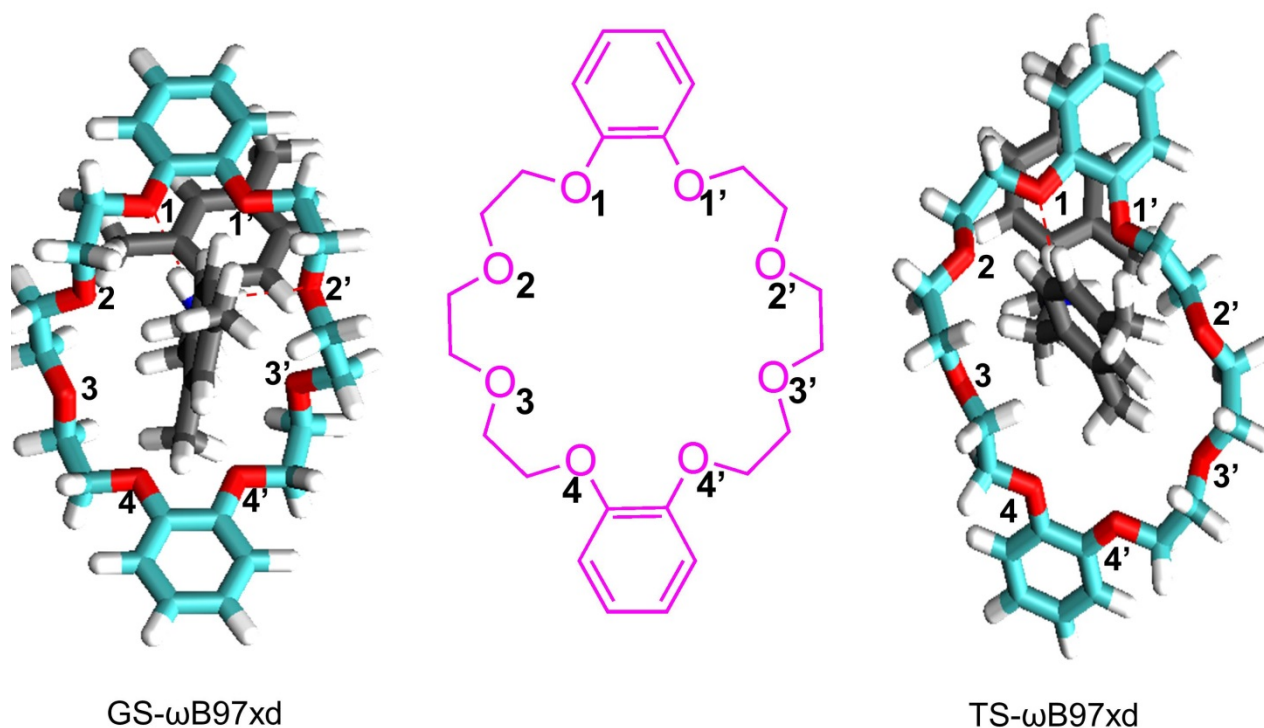
Scheme S1. Structure formula of DB24C8 defining the atom labels in Table S3 (center). Graphical representations evidencing the ring ellipticity in the minimum structure GS ωB97xd (left) and transition state TS ωB97xd (right). Atom colors as in Figure S1. Red dashed lines represent hydrogen bonds.

Distance (Å)	GS ωB97xd	TS ωB97xd	GS PBE-D2	TS PBE-D2	GS-PBE-D2/pw	TS-PBE-D2/pw
O1-O4	7.168	7.200	7.189	7.056	7.241	7.052
O1'-O4'	7.230	7.122	7.230	7.034	7.296	7.044
O2-O2'	5.842	7.513	5.763	7.552	5.876	7.607
O3-O3'	6.059	7.722	6.049	7.845	6.125	7.858
NH$_2$-O2'	1.914		1.842		1.906	
NH$_2$-O1	2.066	1.686	2.064	1.658	2.043	1.671

Table S3. Relevant interatomic distances from static quantum chemical calculations at the ωB97xd D95(d,p) and PBE-D2/D95(d,p) levels for the minimum energy structure of the [6⊂DB24C8]$^+$ complex (GS) and for the transition state structure (TS). Values from geometry optimization with plane waves basis set (PBE-D2/pw) are included for comparison. Atom labels are defined in Scheme S1.

Metadynamics simulation of [10⊂DB24C8]$^+$ in the gas phase

In both guests **5**$^+$ and **10**$^+$, the phenyl rings bear a methoxy substituent in *para* position to the –CH$_2$NH$_2$$^+CH_2$– moiety and a –CH$_3$ substituent in *meta* to the –CH$_2$NH$_2$$^+CH_2$– moiety. Hence, apparently, the phenyl rings of **5**$^+$ and **10**$^+$ do not feature three bulky groups immediately close to each other as *e.g.* in guest **8**$^+$. However, since the –CH$_3$ and –OCH$_3$ substituents are close to each other, the methyl group of –OCH$_3$ points away from the neighboring –CH$_3$ substituent in order to avoid repulsive contacts (see Figure S2, left panel). In this conformation, the steric hindrance of the phenyl rings of guests **5**$^+$ and **10**$^+$ is comparable to that of the stoppers in **8**$^+$. Therefore, for all practical purposes, they should be classified as guests with three substituents around the phenyl ring, which show a "non-threading" behavior in the threading/dethreading experiments.

To test this hypothesis, we selected the **10**$^+$ guest and performed a gas phase metadynamics on the [**10**⊂DB24C8]$^+$ adduct to induce the dethreading of the axle. At the beginning of the simulation, the [**10**⊂DB24C8]$^+$ adduct is fully threaded and the methyl group of the –OCH$_3$ substituent of both phenyl rings of **10**$^+$ points away from the –CH$_3$ substituent in the meta position (Figure S2, left panel). However, in this conformation, the bulkiest part of the phenyl moiety cannot transit through the ring cavity due to the steric hindrance of the close –OCH$_3$ and –CH$_3$ substituents (Figure S2, center panel). Indeed, **10**$^+$ could exit the ring only if the methoxy group of the transiting phenyl moiety performs an energetically expensive rotation around its C–O axis. This reorientation brings –OCH$_3$ in very close contact with the methyl substituent (Figure S2, right panel).
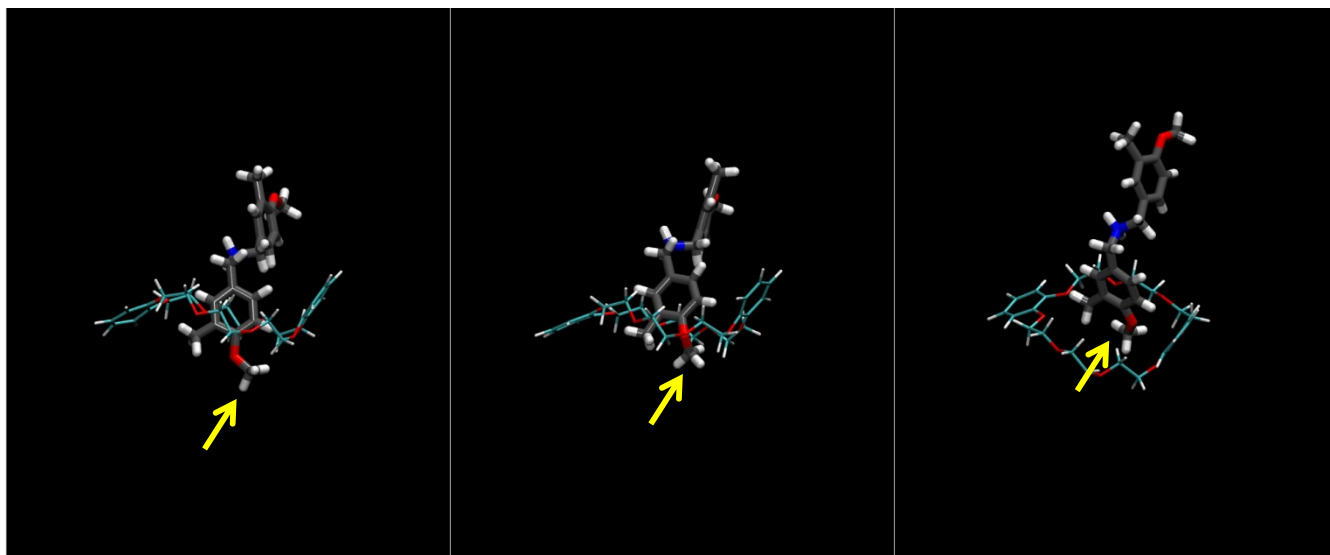
Figure S2. Three snapshots of the (gas-phase) metadynamics simulation of the dethreading of the [**10**⊂DB24C8]$^+$ complex. Left panel: fully threaded complex. Center panel: partially dethreaded complex: the –OCH$_3$ group starts to reorient in order to allow the transit of the phenyl moiety through the macrocycle. In the dethreaded complex (right panel) the methoxy substituent of the phenyl group has rotated around the C–O axis, and is in very close contact with the neighboring –CH$_3$ substituent. Color codes: C (ring) = cyan; C(axle) = grey; N = blue; O = red; H = white. The yellow arrows indicate the OCH$_3$ group undergoing the reorientation.

Such a conformation should be strongly destabilized by repulsive interactions, and therefore very unlikely to occur.

Hence, the results of the metadynamics simulation strongly suggest that the passage of guests **5**$^+$ and **10**$^+$ through the macrocycle should not take place, because it would require drastic and energetically unfavourable conformational changes of the axle moieties.

4. UV-Vis characterization

Absorption spectra
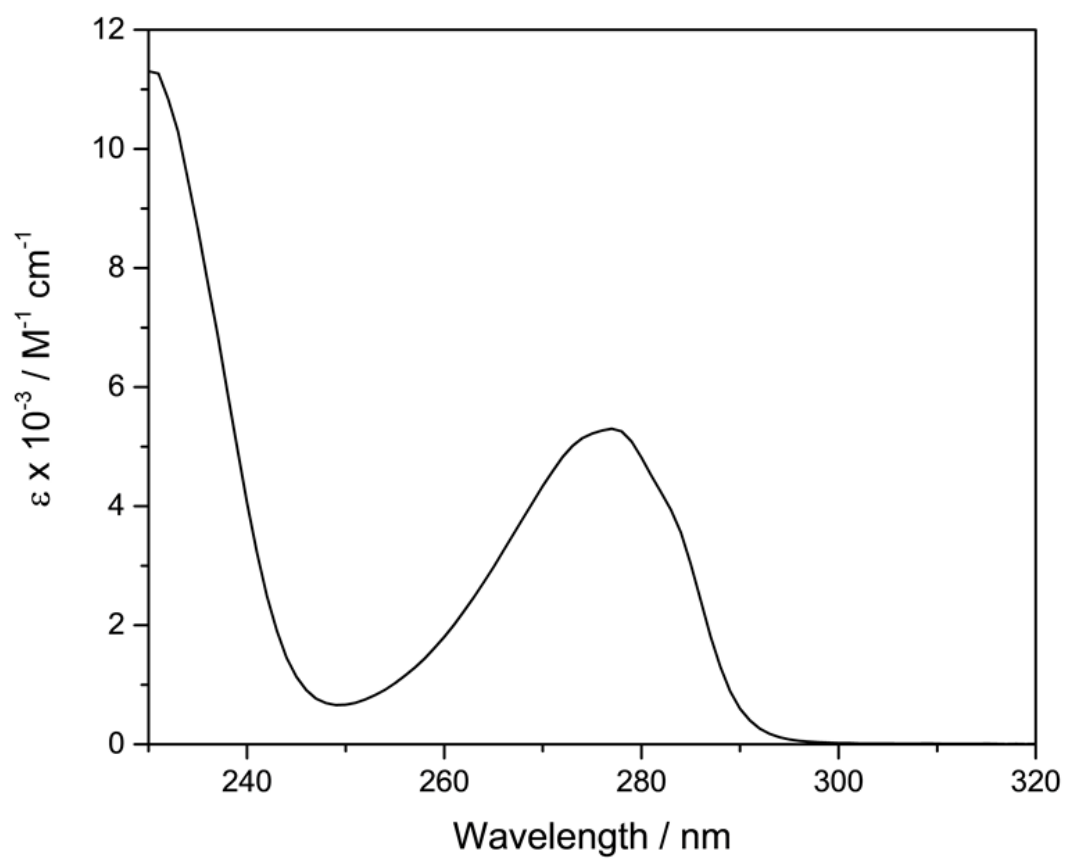
Figure S3. Absorption spectrum of DB24C8 in CH_2Cl_2.
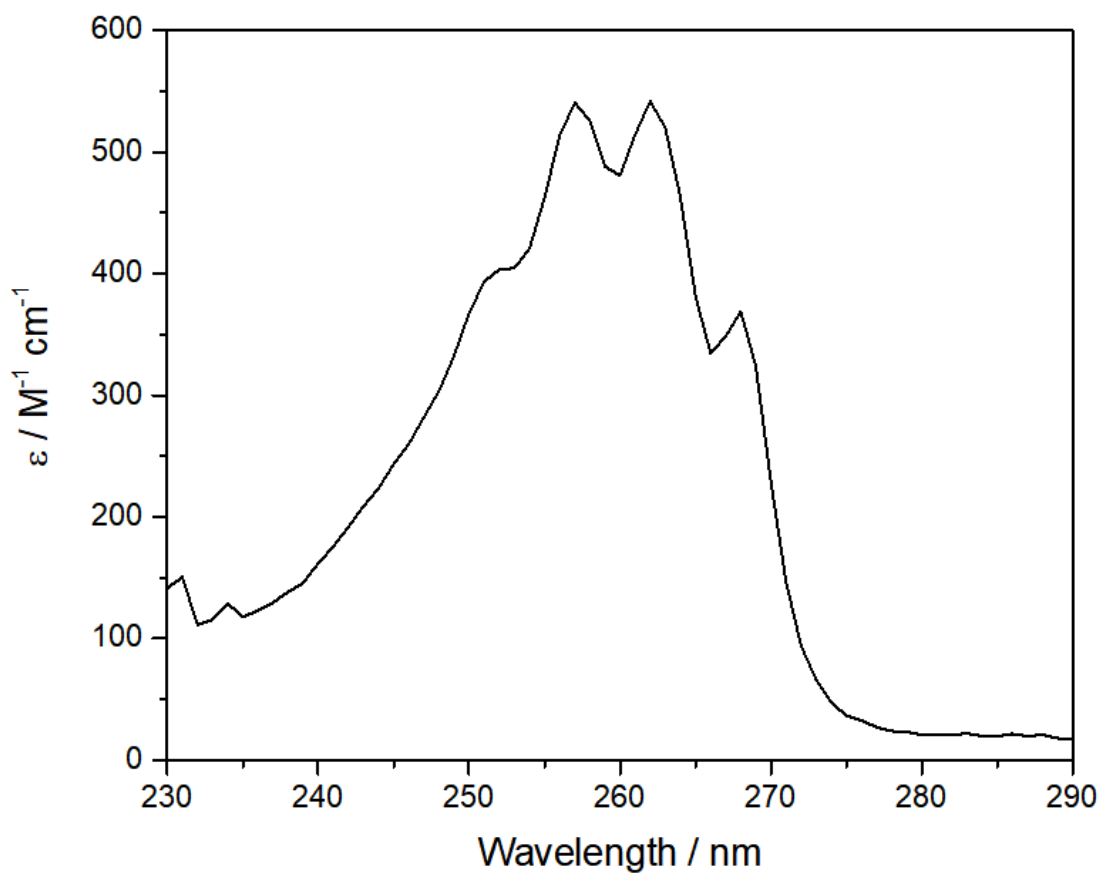
Figure S4. Absorption spectrum of compound **1**$^+$ in CH_2Cl_2.
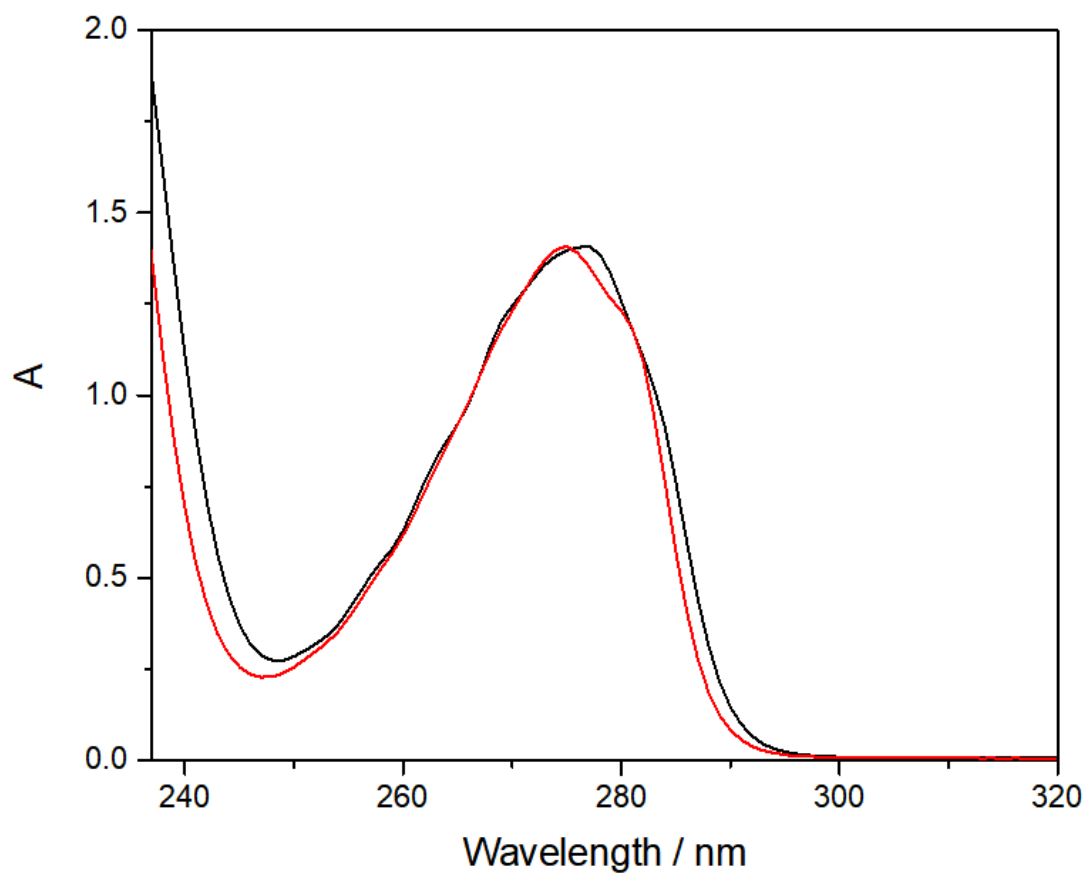
Figure S5. Sum of the absorption spectra of separated CH_2Cl_2 solutions of DB24C8 and $\mathbf{1}^+$ (black line) and absorption spectrum of the same solutions after mixing (red line). Concentrations in the mixture: $[DB24C8] = 2.8 \times 10^{-4}$ M, $[\mathbf{1}^+] = 3.1 \times 10^{-4}$ M.
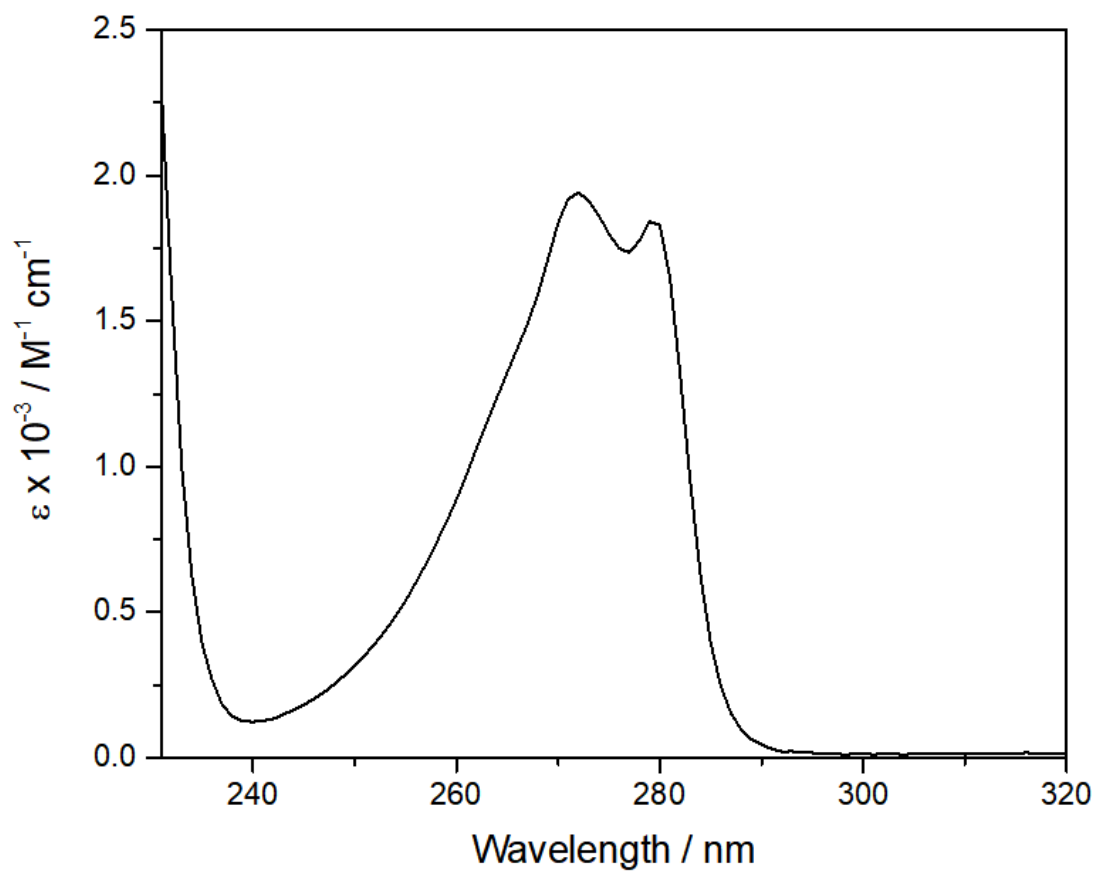
Figure S6. Absorption spectrum of compound **4**[+] in CH_2Cl_2.
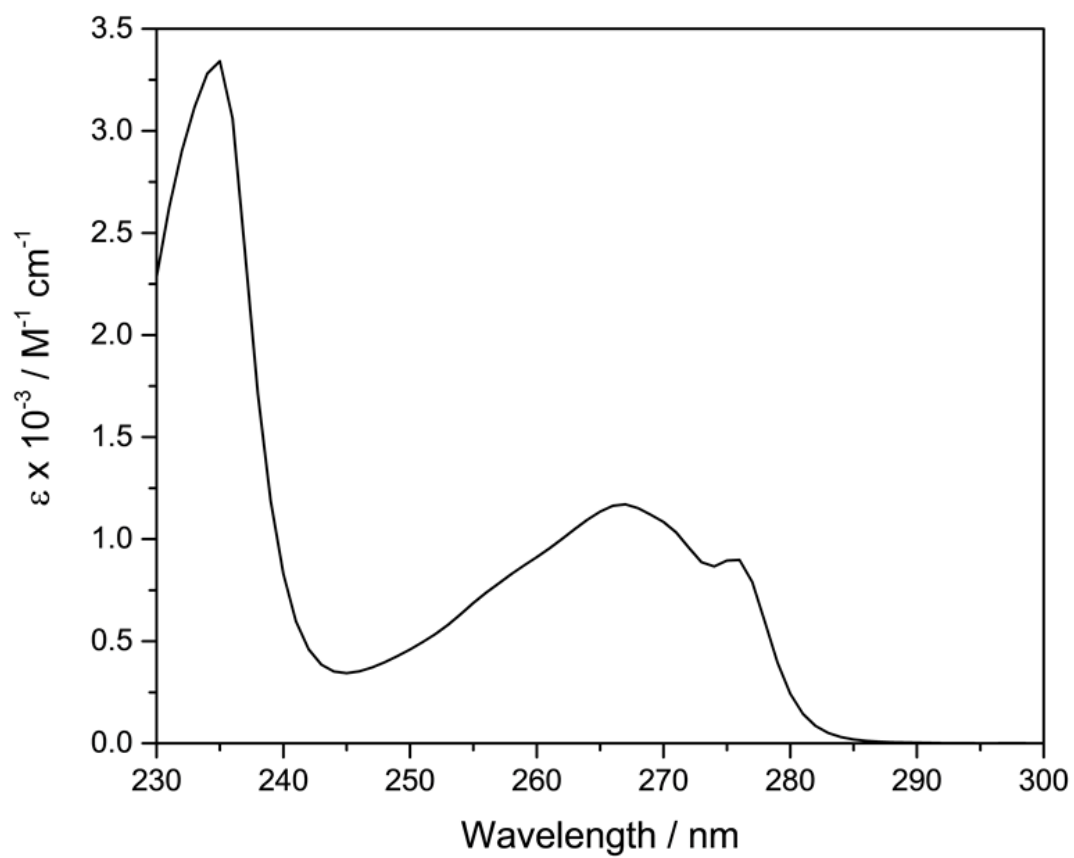
Figure S7. Absorption spectrum of compound **6**$^+$ in CH_2Cl_2.
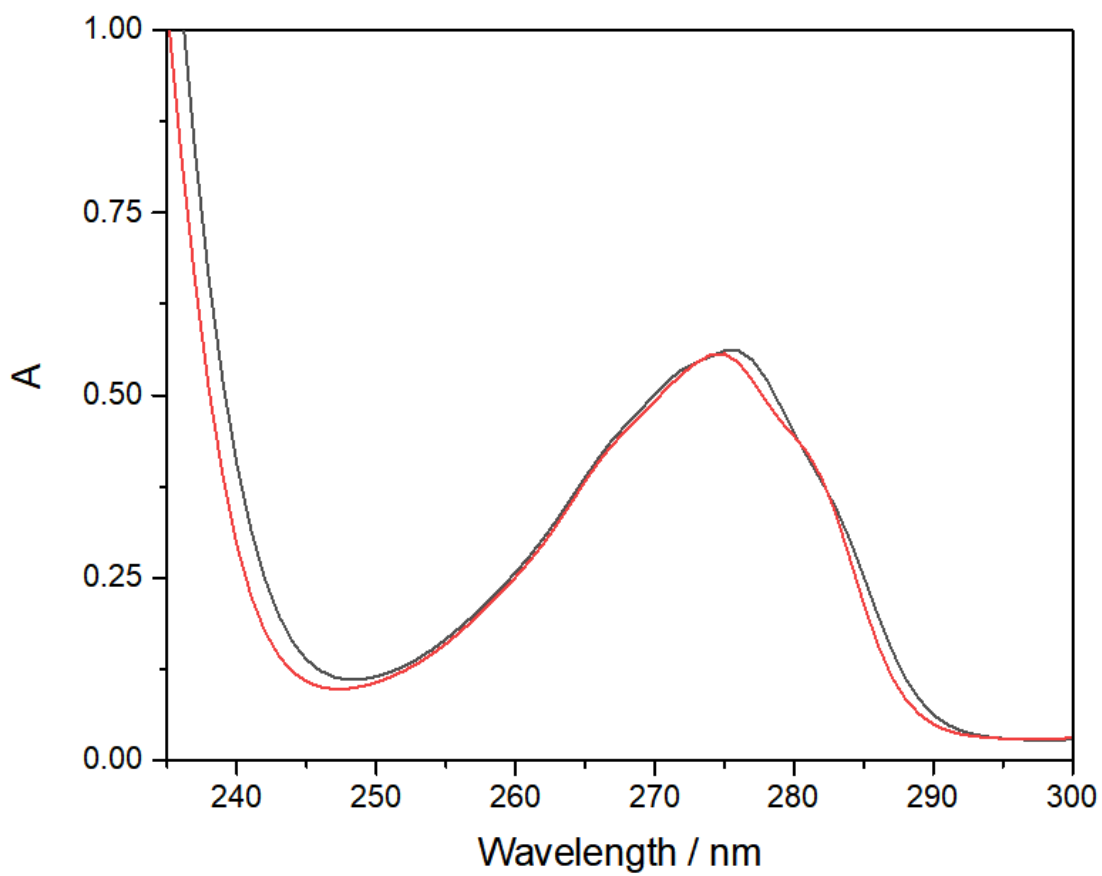
Figure S8. Sum of the absorption spectra of separated CH_2Cl_2 solutions of DB24C8 and **6**$^+$ (black line) and absorption spectrum of the same solutions after mixing (red line). Concentrations in the mixture: [DB24C8] = [**6**$^+$] = 5.5×10^{-5} M.
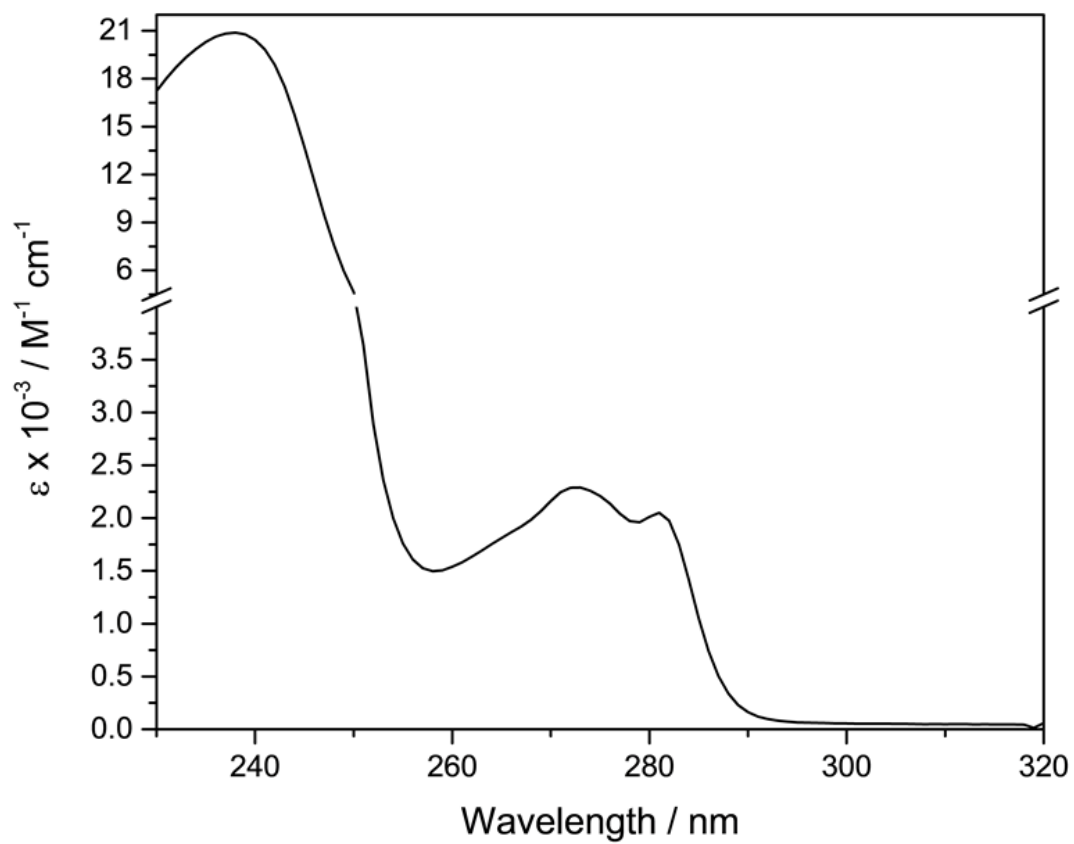
Figure S9. Absorption spectrum of compound 7^+ in CH_2Cl_2.
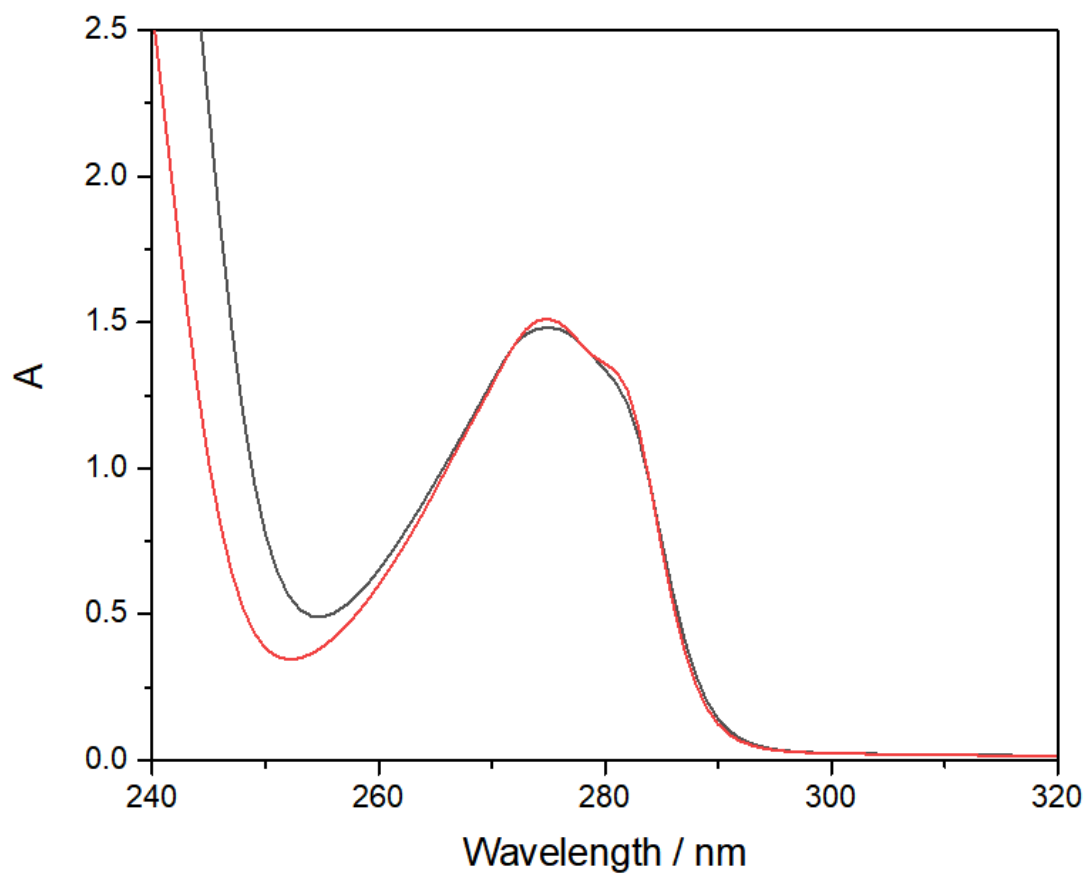
Figure S10. Sum of the absorption spectra of separated CH_2Cl_2 solutions of DB24C8 and $\mathbf{7}^+$ (black line) and absorption spectrum of the same solutions after mixing (red line). Concentrations in the mixture: $[DB24C8] = [\mathbf{7}^+] = 1.84 \times 10^{-4}$ M.

5. Thermodynamic and kinetic characterization

UV-Vis titration experiments
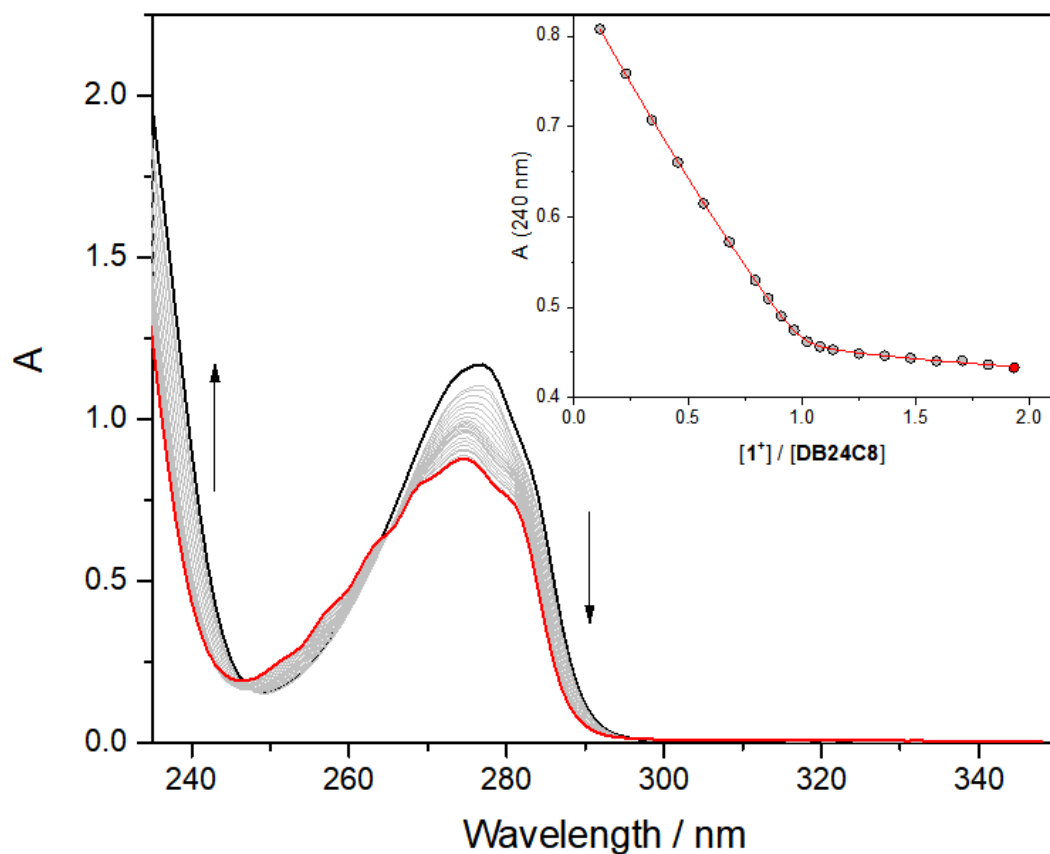
Figure S11. Absorption spectra of a 2.2×10^{-4} M solution of DB24C8 in CH_2Cl_2 upon addition of $\mathbf{1}^+$. The inset shows the absorption changes at 240 nm together with the fitted curve corresponding to a 1:1 binding model.
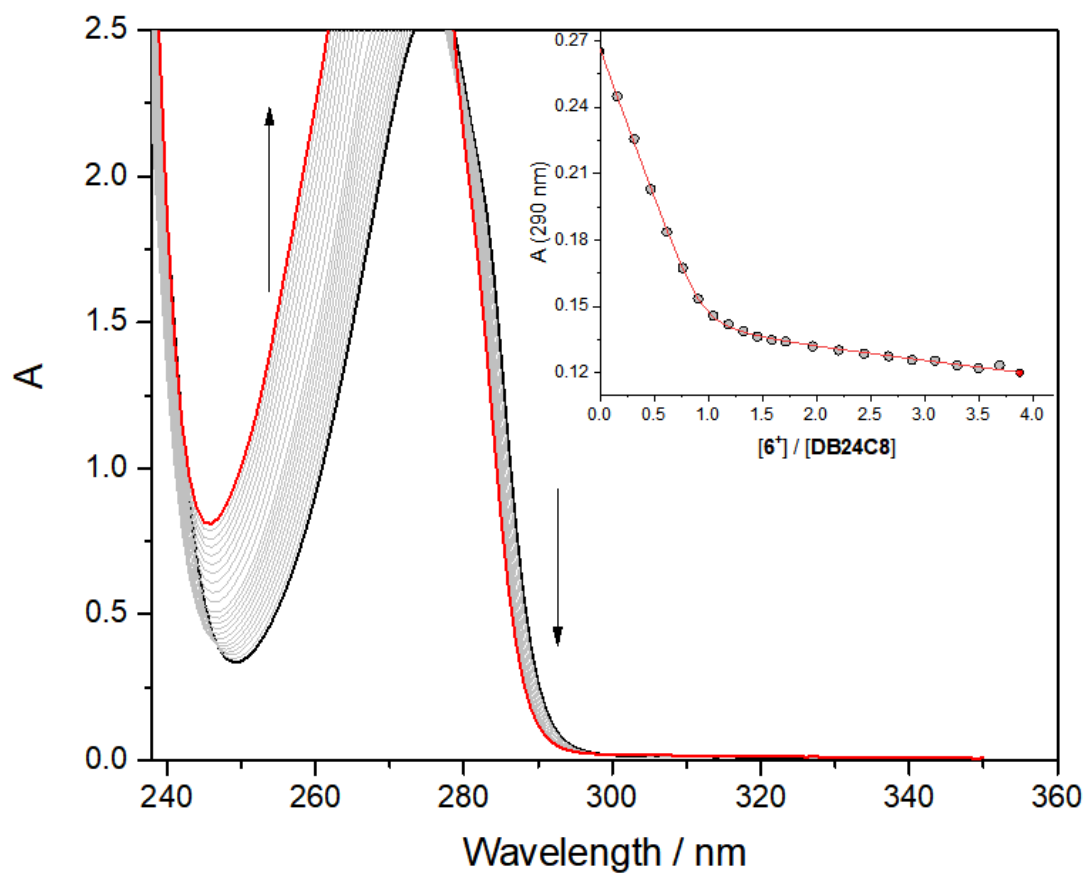
Figure S12. Absorption spectra of a 4.5×10⁻⁴ M solution of DB24C8 in CH$_2$Cl$_2$ upon addition of **6**⁺. The inset shows the absorption changes at 290 nm together with the fitted curve corresponding to a 1:1 binding model.
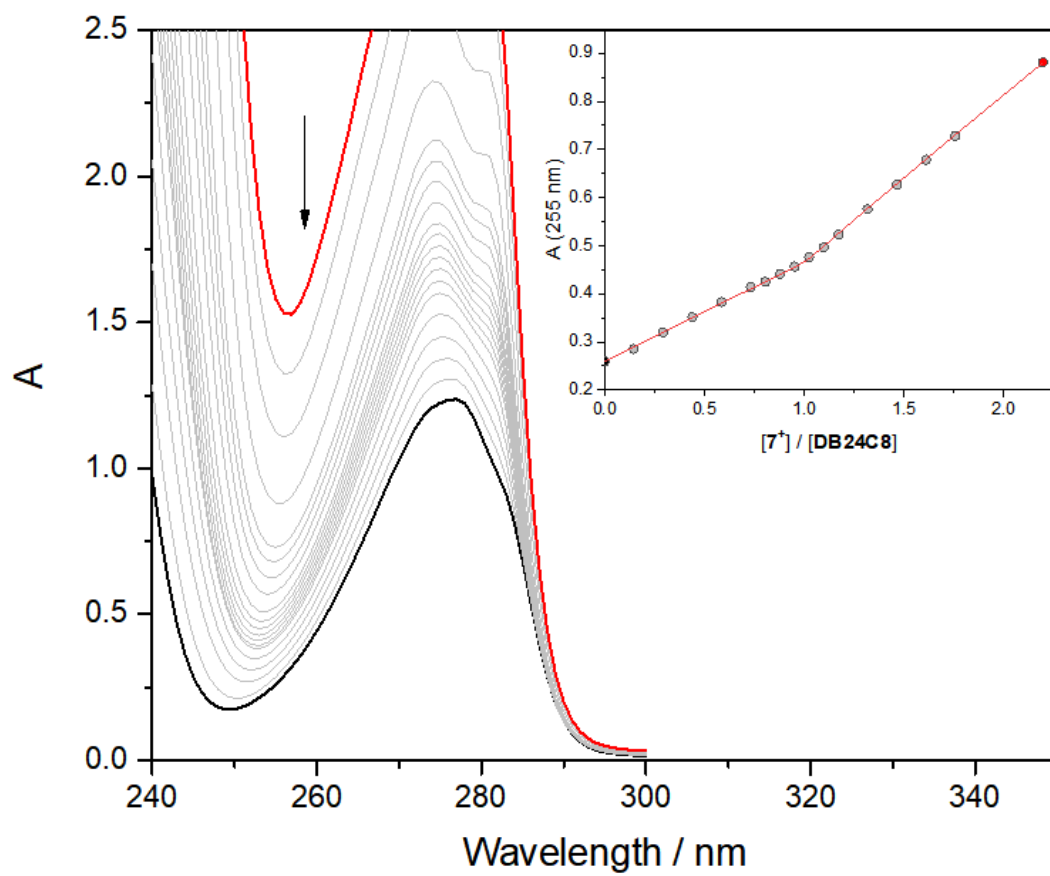
Figure S13. Absorption spectra of a 2.5×10^{-4} M solution of DB24C8 in CH_2Cl_2 upon addition of **7**$^+$. The inset shows the absorption changes at 255 nm together with the fitted curve corresponding to a 1:1 binding model.

UV-Vis kinetic experiments
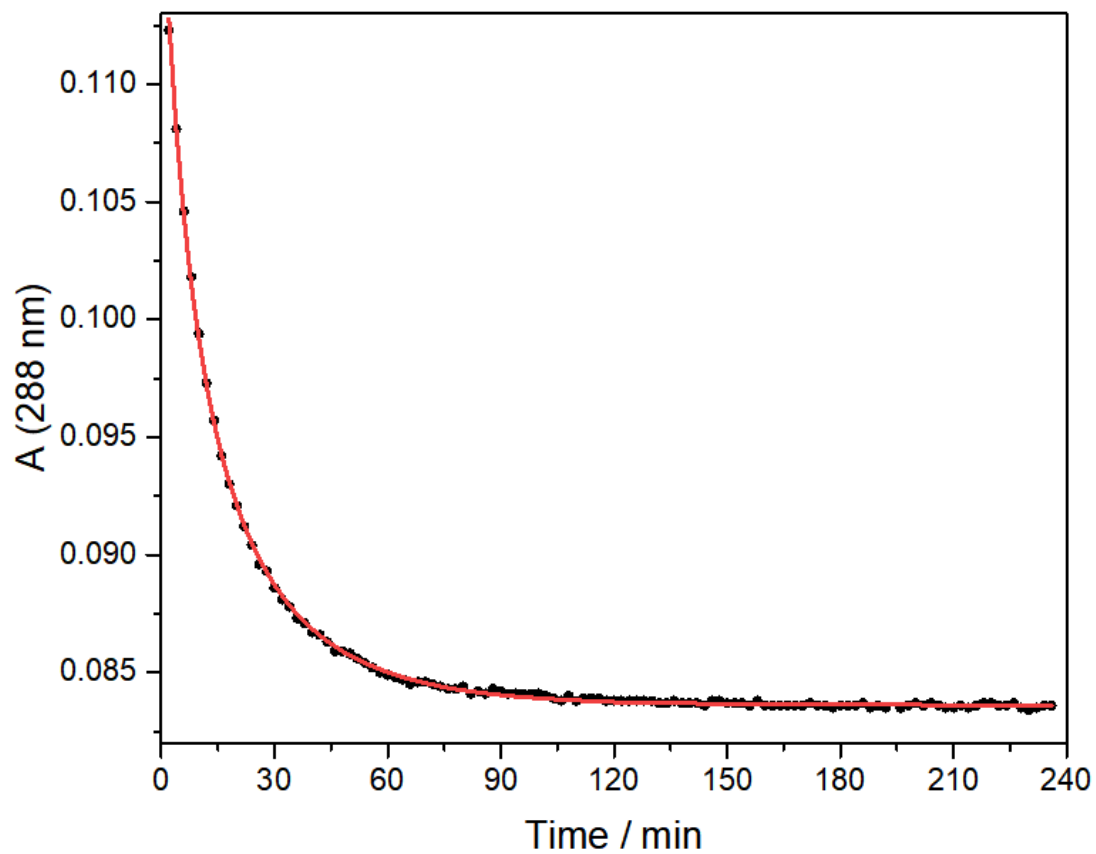
Figure S14. Time-dependent absorption changes at 288 nm recorded upon mixing DB24C8 and **6**$^+$ in CH$_2$Cl$_2$ at 298 K. Concentrations after mixing: [DB24C8] = [**6**$^+$] = 1.0×10^{-4} M. The red solid line represents the data fitting.
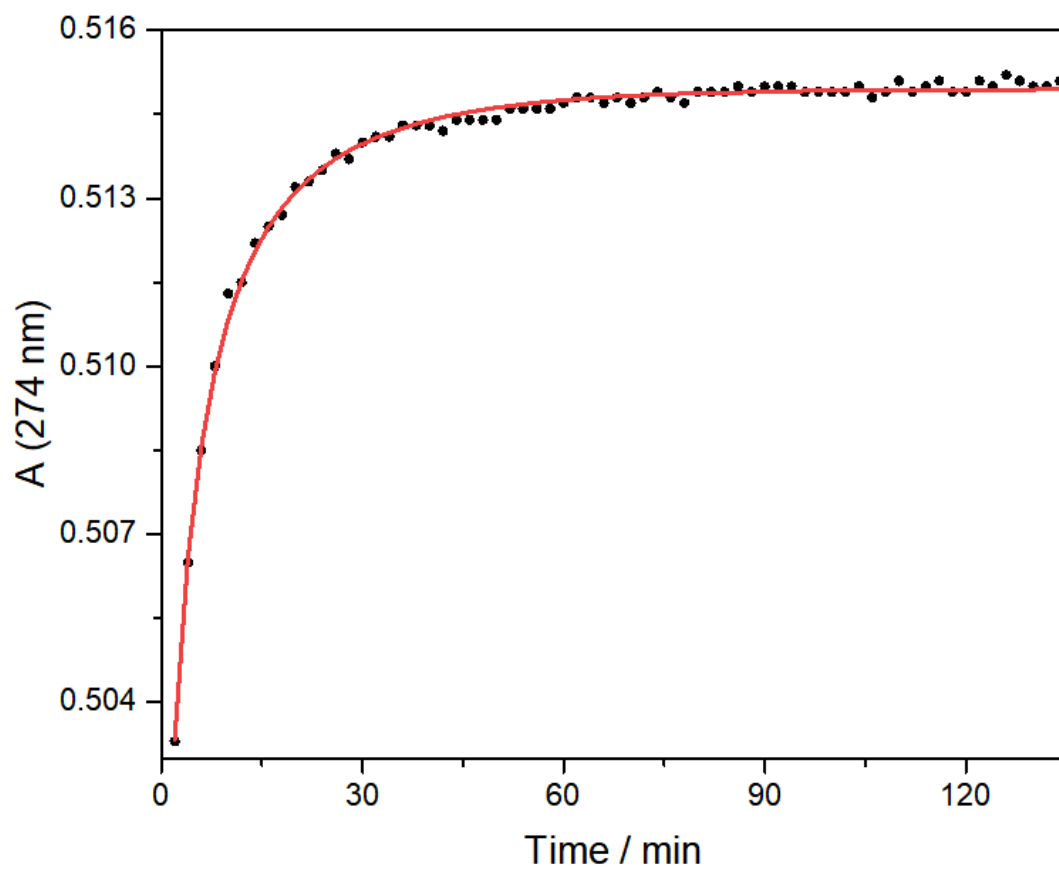
Figure S15. Time-dependent absorption changes at 274 nm recorded upon mixing DB24C8 and $\mathbf{7}^+$ in CH$_2$Cl$_2$ at 298 K. Concentrations after mixing: [DB24C8] = [$\mathbf{7}^+$] = 7.8×10^{-5} M. The red solid line represents the data fitting.
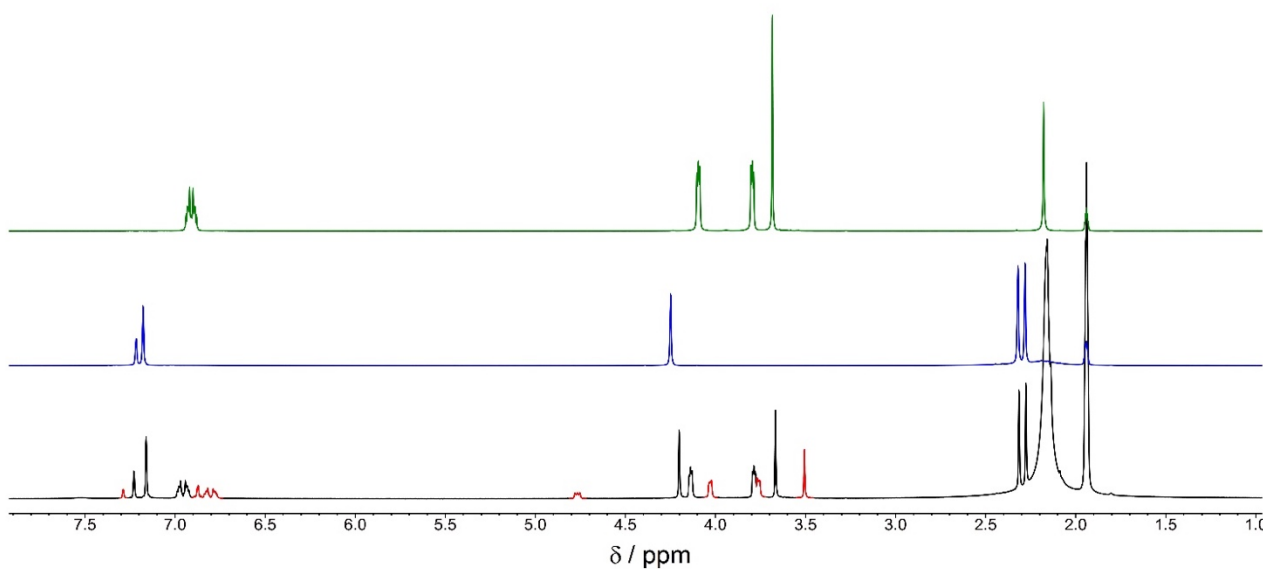
6. ¹H NMR Spectroscopy

Complexation studies in CD₃CN
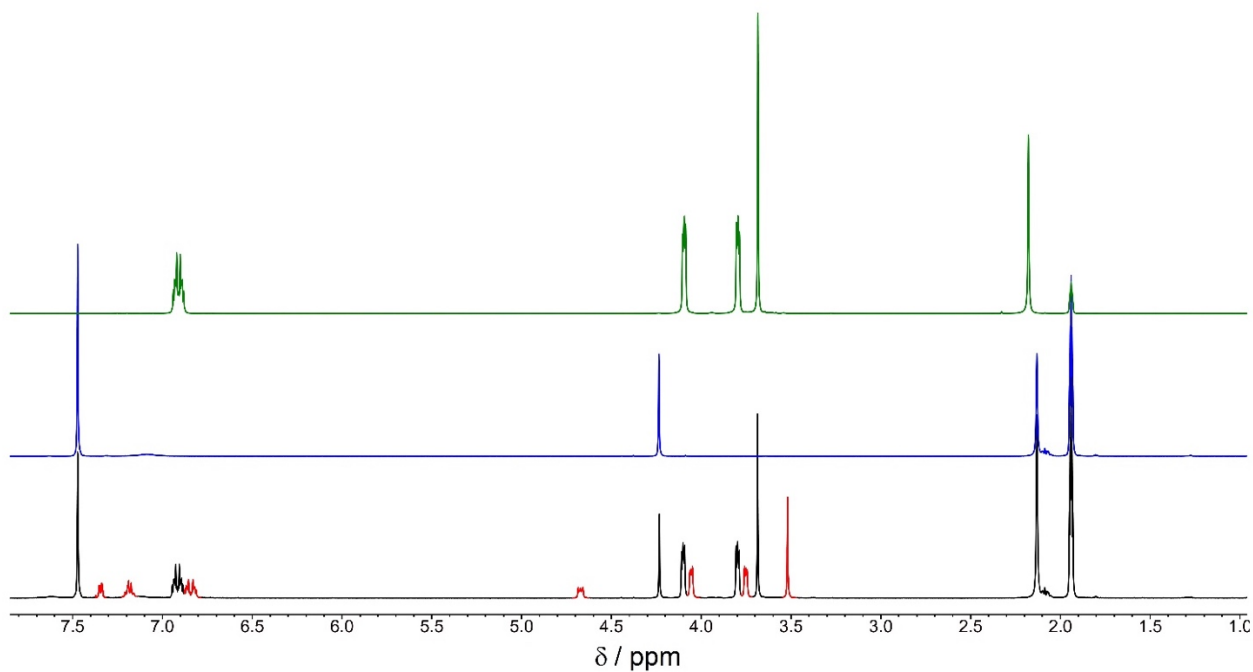
Figure S16. ¹H NMR spectra (500 MHz, 298 K, CD₃CN) of a solution of a 1:1 mixture of **1**⁺ and DB24C8 (3 mM) (black line), the signals associated with the complex are highlighted in red, a solution of **1**⁺ (3 mM) (blue line) and a solution of DB24C8 (3 mM) (green line).
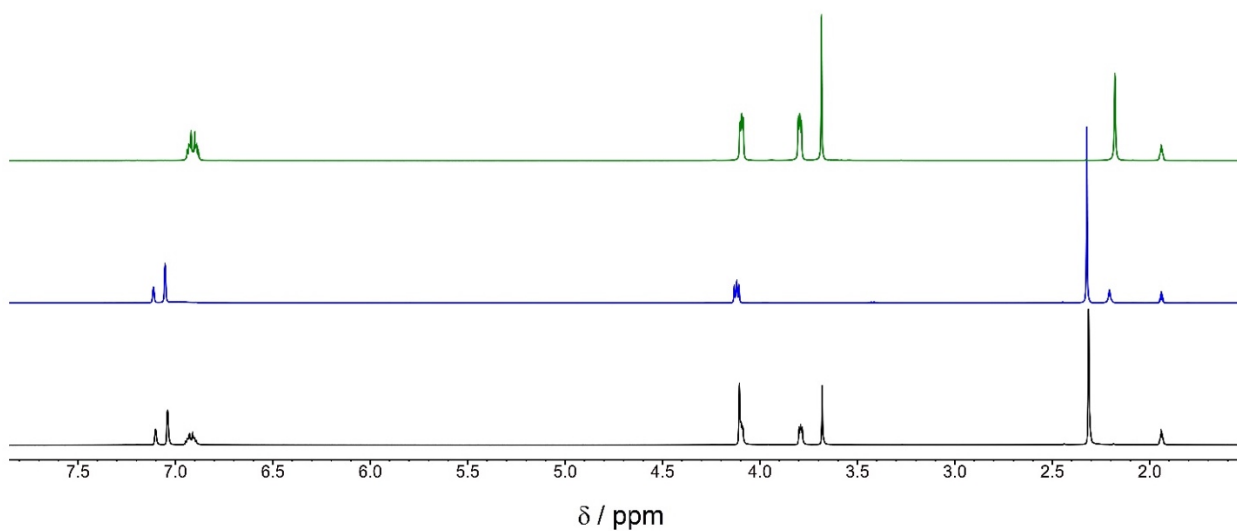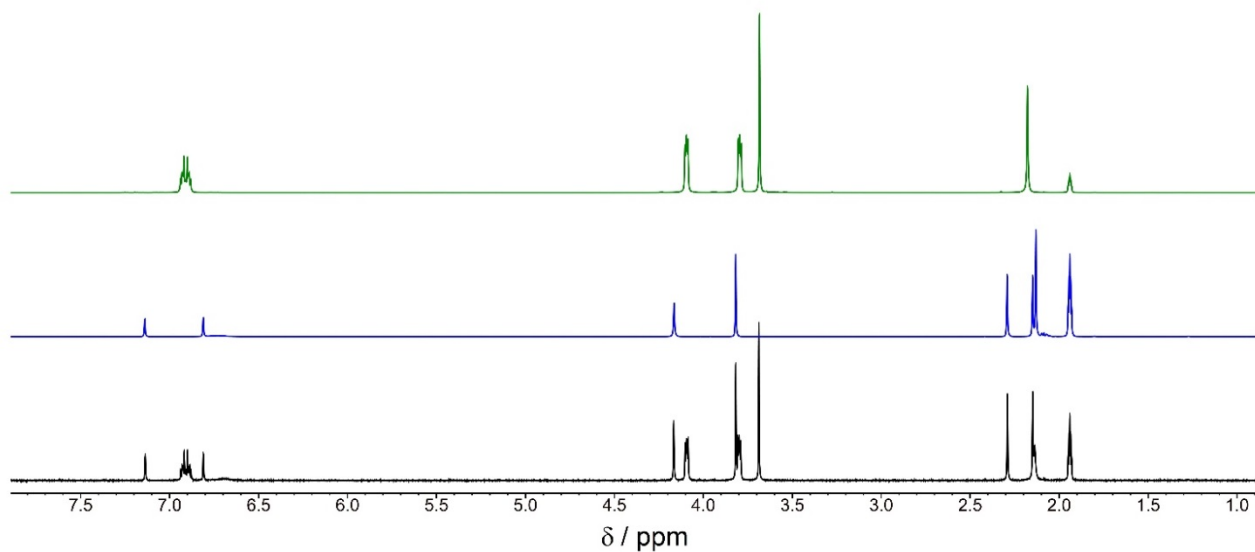

Figure S17. ¹H NMR spectra (500 MHz, 298 K, CD₃CN) of a solution of a 1:1 mixture of **2**⁺ and DB24C8 (3 mM) (black line), the signals associated with the complex are highlighted in red, a solution of **2**⁺ (3 mM) (blue line) and a solution of DB24C8 (3 mM) (green line).
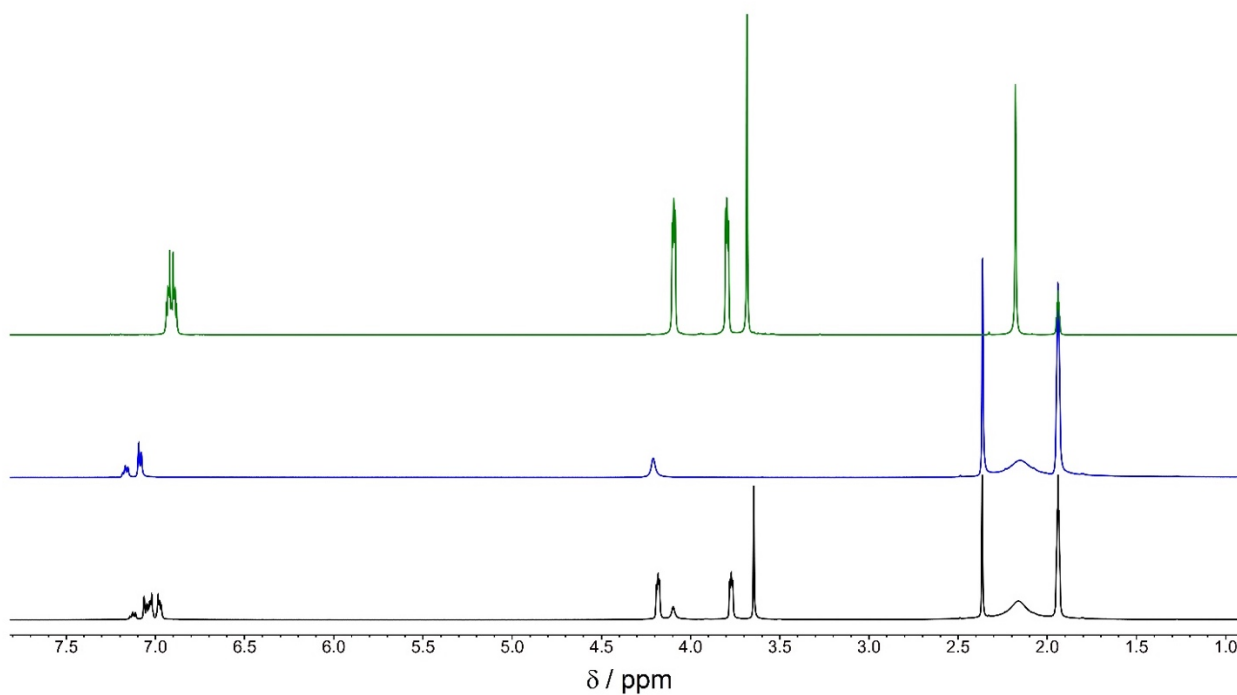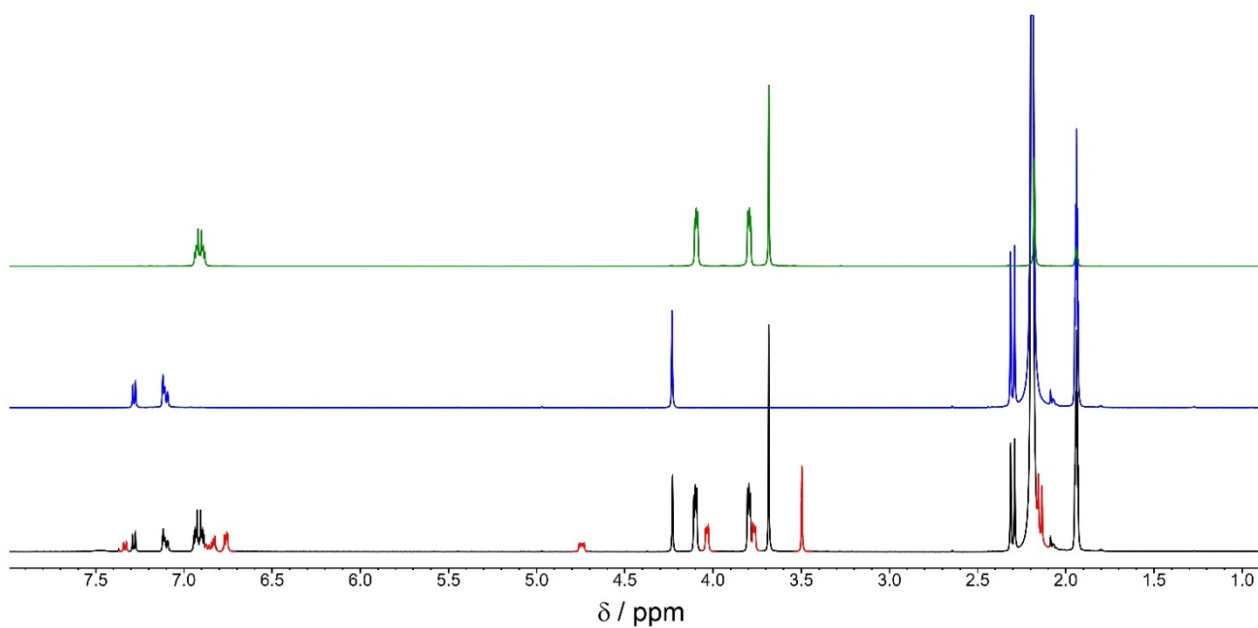
Figure S18. ^{1}H NMR spectra (500 MHz, 298 K, CD$_3$CN) of a solution of a 1:1 mixture of **3**$^+$ and DB24C8 (3 mM) (black line), the signals associated with the complex are highlighted in red, a solution of **3**$^+$ (3 mM) (blue line) and a solution of DB24C8 (3 mM) (green line).
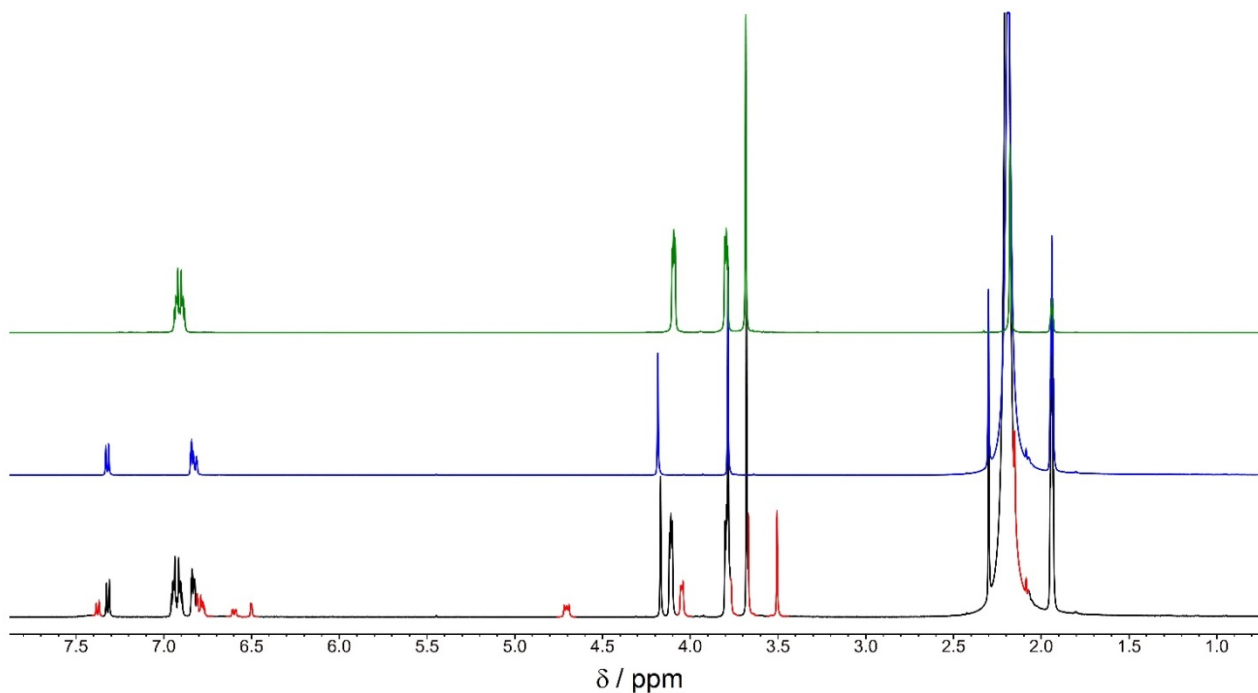

Figure S19. ^{1}H NMR spectra (500 MHz, 298 K, CD$_3$CN) of a solution of a 1:1 mixture of **4**$^+$ and DB24C8 (3 mM) (black line), the signals associated with the complex are highlighted in red, a solution of **4**$^+$ (3 mM) (blue line) and a solution of DB24C8 (3 mM) (green line).
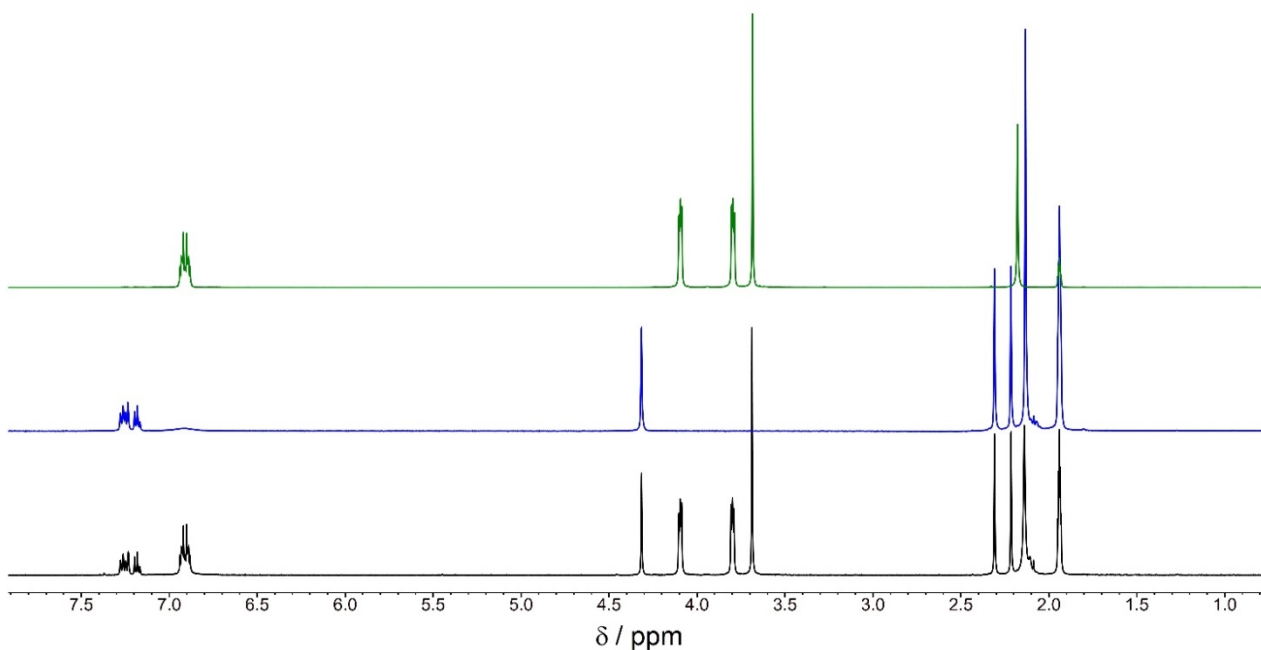
Figure S20. ^{1}H NMR spectra (500 MHz, 298 K, CD$_3$CN) of a solution of a 1:1 mixture of **5**$^+$ and DB24C8 (3 mM) (black line), the signals associated with the complex are highlighted in red, a solution of **5**$^+$ (3 mM) (blue line) and a solution of DB24C8 (3 mM) (green line).

Figure S21. ^{1}H NMR spectra (500 MHz, 298 K, CD$_3$CN) of a solution of a 1:1 mixture of **6**$^+$ and DB24C8 (3 mM) (black line), the signals associated with the complex are highlighted in red, a solution of **6**$^+$ (3 mM) (blue line) and a solution of DB24C8 (3 mM) (green line).
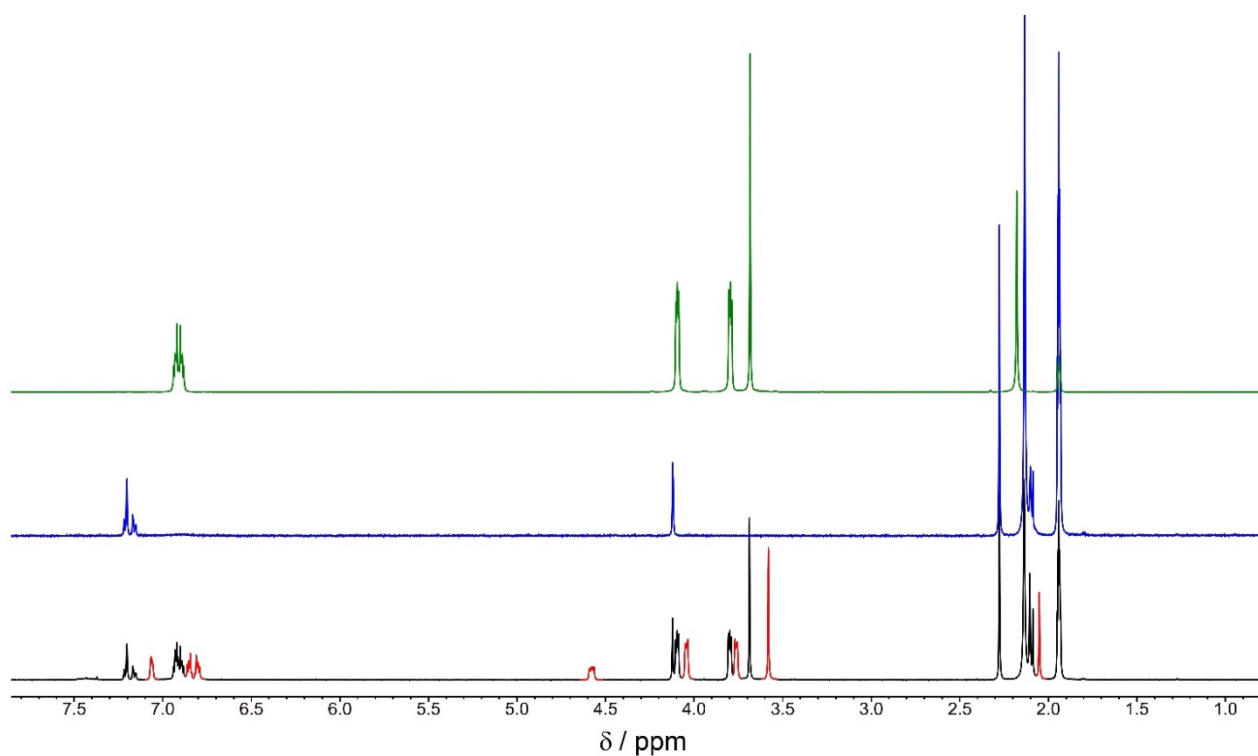
Figure S22. ^{1}H NMR spectra (500 MHz, 298 K, CD$_{3}$CN) of a solution of a 1:1 mixture of **7**$^{+}$ and DB24C8 (3 mM) (black line), the signals associated with the complex are highlighted in red, a solution of **7**$^{+}$ (3 mM) (blue line) and a solution of DB24C8 (3 mM) (green line).
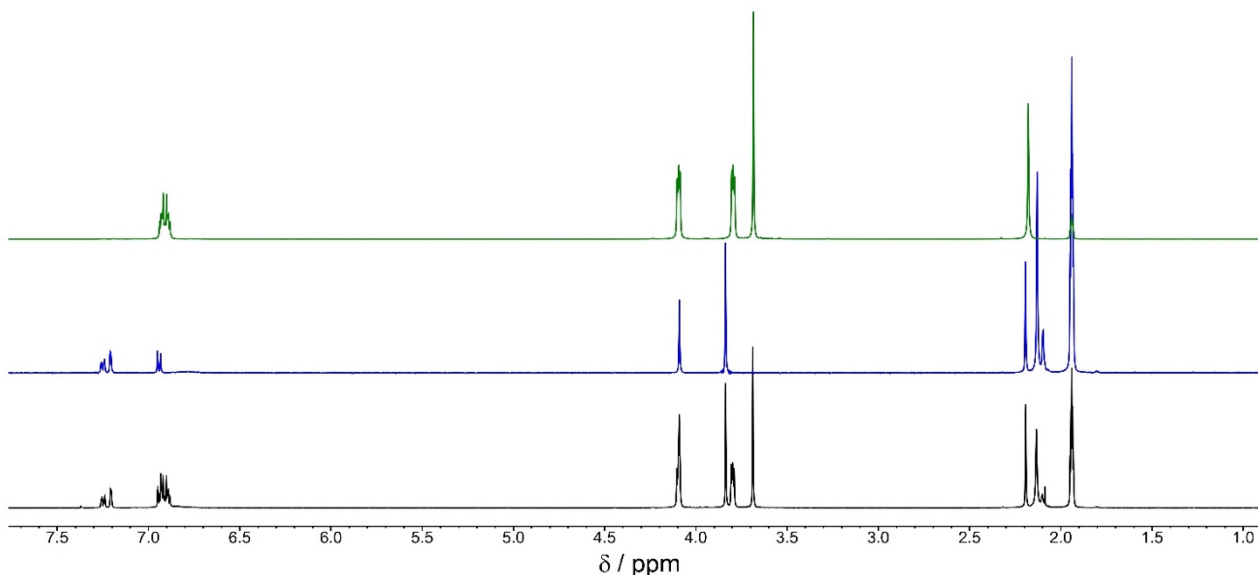

Figure S23. ^{1}H NMR spectra (500 MHz, 298 K, CD$_{3}$CN) of a solution of a 1:1 mixture of **8**$^{+}$ and DB24C8 (3 mM) (black line), the signals associated with the complex are highlighted in red, a solution of **8**$^{+}$ (3 mM) (blue line) and a solution of DB24C8 (3 mM) (green line).
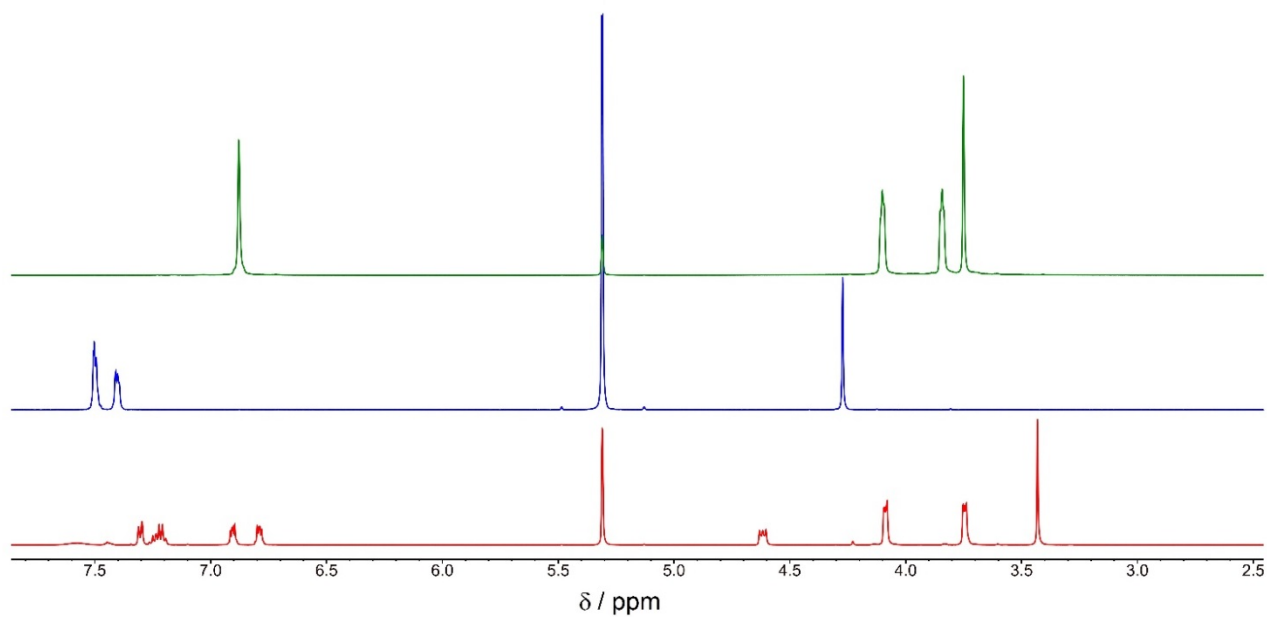
Figure S24. ^{1}H NMR spectra (500 MHz, 298 K, CD$_3$CN) of a solution of a 1:1 mixture of **9**[+] and DB24C8 (3 mM) (black line), the signals associated with the complex are highlighted in red, a solution of **9**[+] (3 mM) (blue line) and a solution of DB24C8 (3 mM) (green line).

Figure S25. ^{1}H NMR spectra (500 MHz, 298 K, CD$_3$CN) of a solution of a 1:1 mixture of **10**[+] and DB24C8 (3 mM) (black line), the signals associated with the complex are highlighted in red, a solution of **10**[+] (3 mM) (blue line) and a solution of DB24C8 (3 mM) (green line).
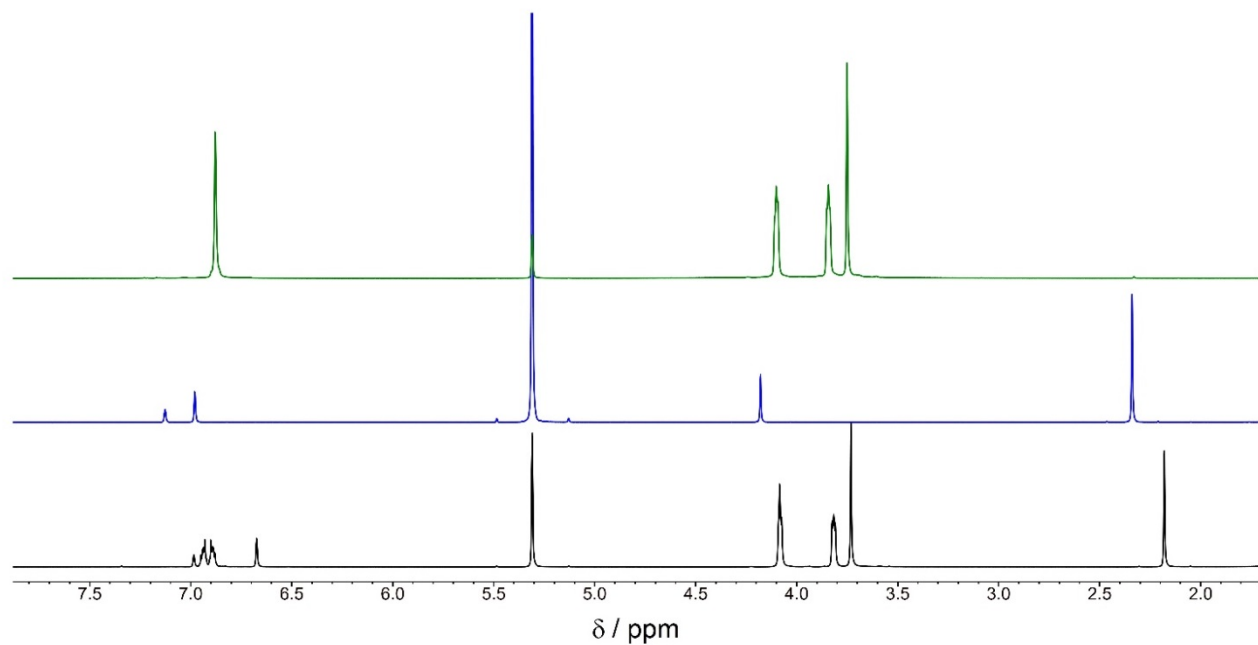
Complexation studies in CD₂Cl₂

Figure S26. ¹H NMR spectra (500 MHz, 298 K, CD₂Cl₂) of a solution of a 1:1 mixture of **1⁺** and DB24C8 (3 mM) (black line), the signals associated with the complex are highlighted in red, a solution of **1⁺** (3 mM) (blue line) and a solution of DB24C8 (3 mM) (green line).
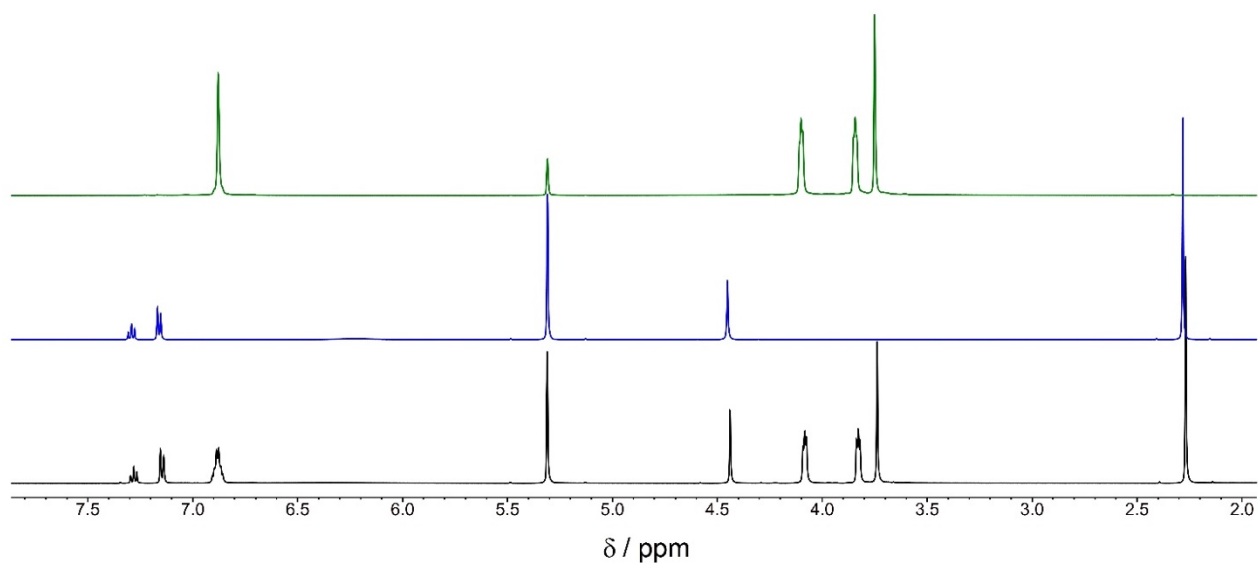

Figure S27. ¹H NMR spectra (500 MHz, 298 K, CD₂Cl₂) of a solution of a 1:1 mixture of **2⁺** and DB24C8 (3 mM) (black line), the signals associated with the complex are highlighted in red, a solution of **2⁺** (3 mM) (blue line) and a solution of DB24C8 (3mM) (green line).
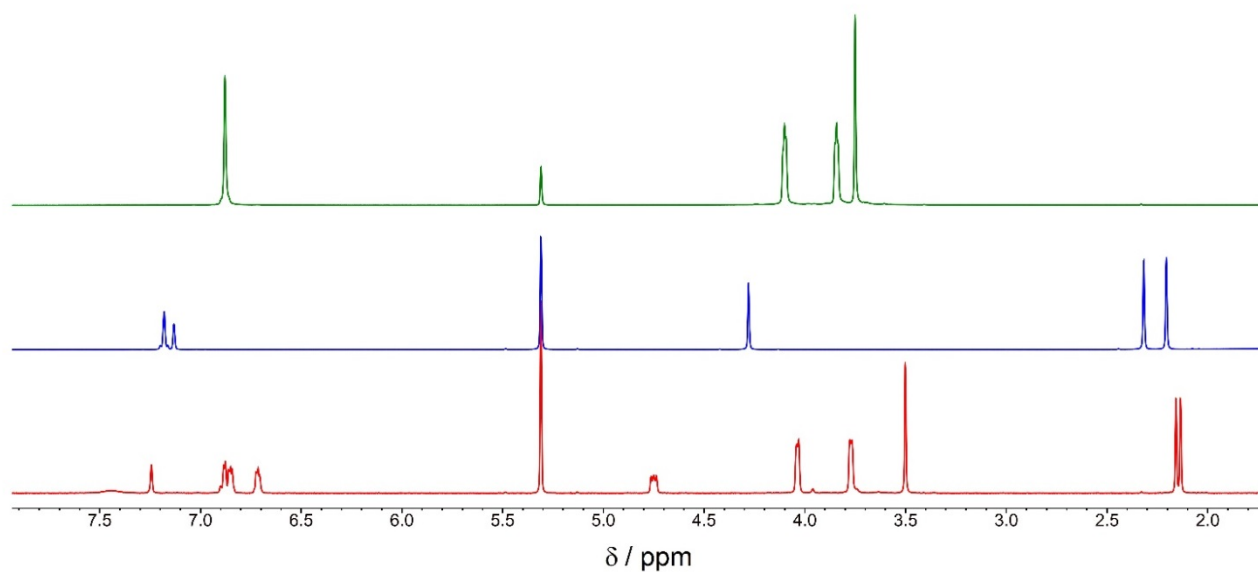
Figure S28. ¹H NMR spectra (500 MHz, 298 K, CD₂Cl₂) of a solution of a 1:1 mixture of **3⁺** and DB24C8 (3 mM) (black line), the signals associated with the complex are highlighted in red, a solution of **3⁺** (3 mM) (blue line) and a solution of DB24C8 (3 mM) (green line).

Figure S29. ¹H NMR spectra (500 MHz, 298 K, CD₂Cl₂) of a solution of a 1:1 mixture of **4⁺** and DB24C8 (3 mM) (black line), the signals associated with the complex are highlighted in red, a solution of **4⁺** (3 mM) (blue line) and a solution of DB24C8 (3 mM) (green line).
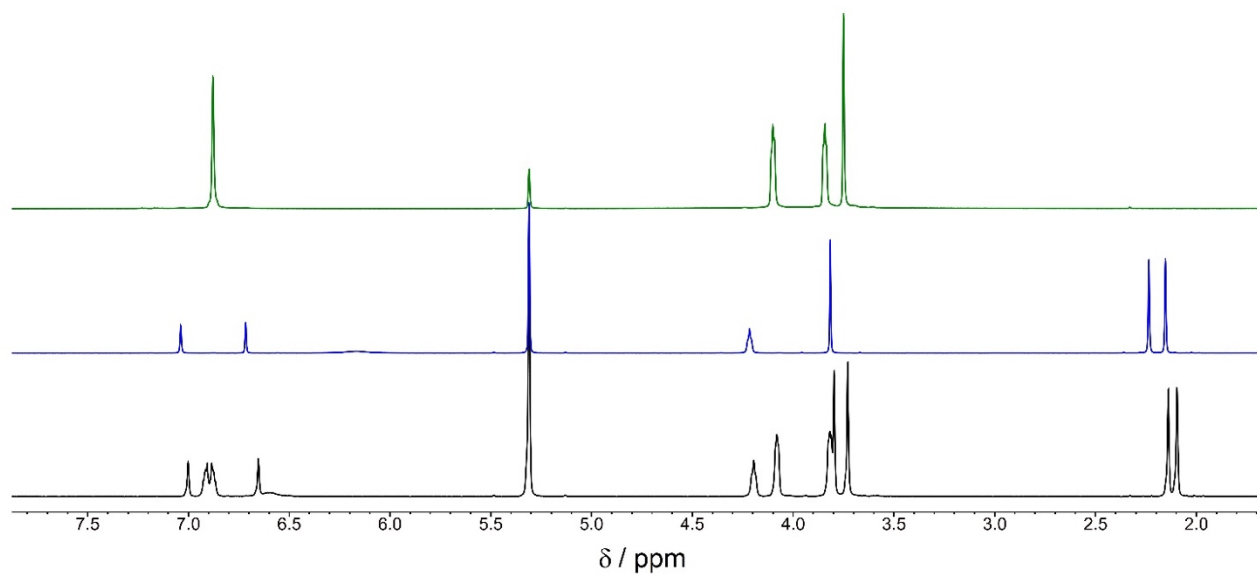
Figure S30. ^{1}H NMR spectra (500 MHz, 298 K, CD$_2$Cl$_2$) of a solution of a 1:1 mixture of **5**$^+$ and DB24C8 (3 mM) (black line), the signals associated with the complex are highlighted in red, a solution of **5**$^+$ (3 mM) (blue line) and a solution of DB24C8 (3 mM) (green line).
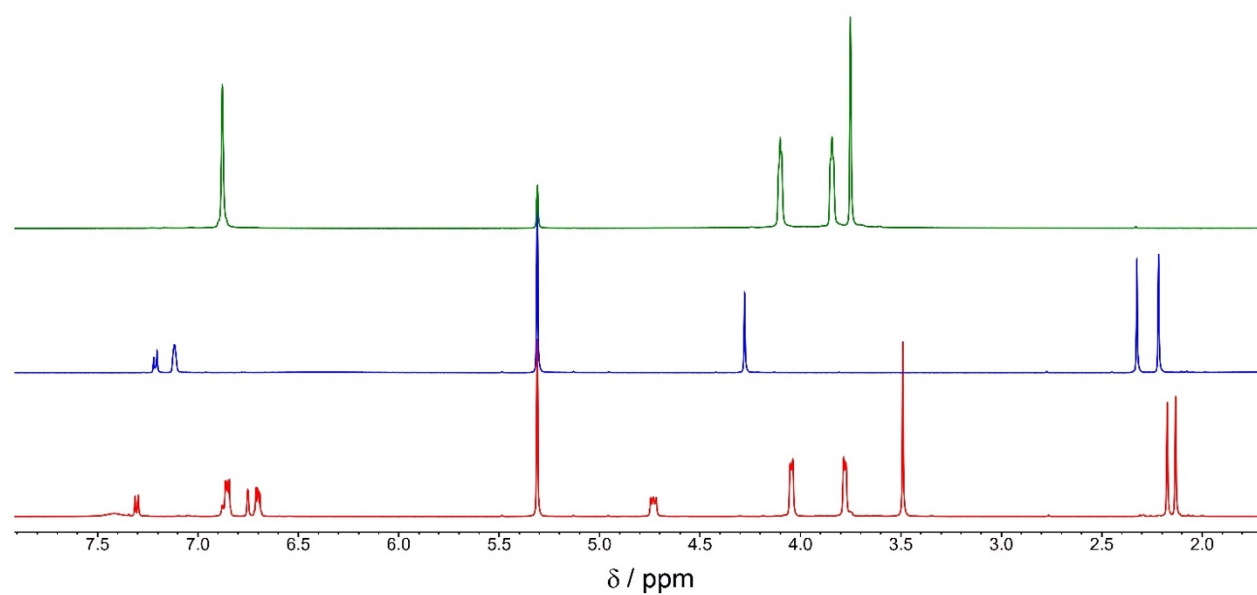

Figure S31. ^{1}H NMR spectra (500 MHz, 298 K, CD$_2$Cl$_2$) of a solution of a 1:1 mixture of **6**$^+$ and DB24C8 (3 mM) (black line), the signals associated with the complex are highlighted in red, a solution of **6**$^+$ (3 mM) (blue line) and a solution of DB24C8 (3 mM) (green line).

Figure S32. ^{1}H NMR spectra (500 MHz, 298 K, CD$_2$Cl$_2$) of a solution of a 1:1 mixture of **7**$^+$ and DB24C8 (3 mM) (black line), the signals associated with the complex are highlighted in red, a solution of **7**$^+$ (3 mM) (blue line) and a solution of DB24C8 (3 mM) (green line).
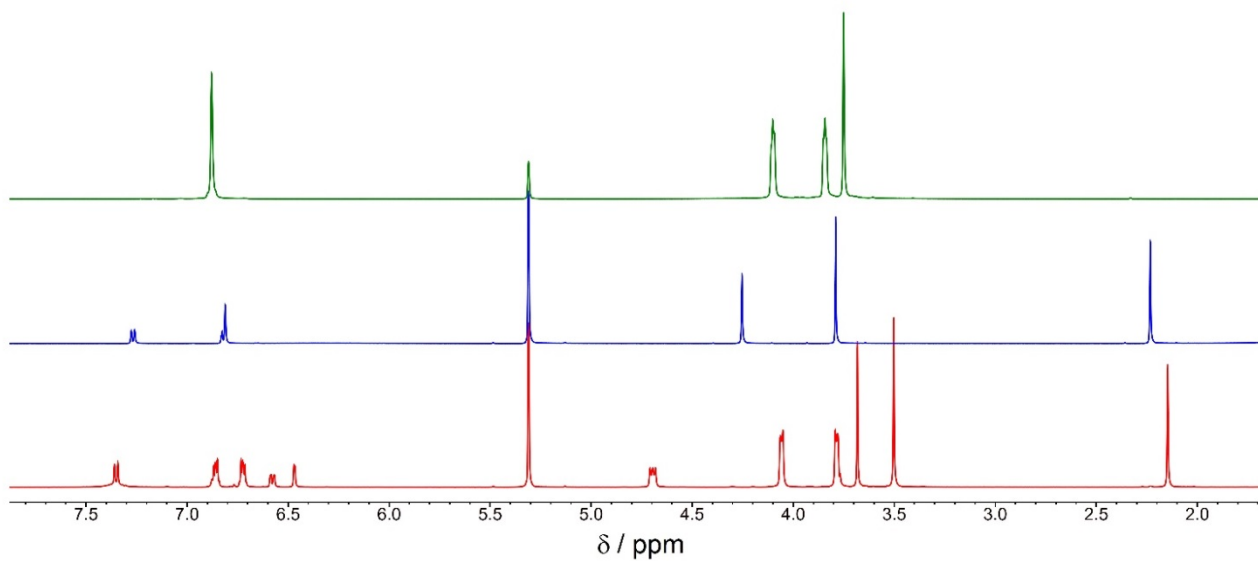

Figure S33. ^{1}H NMR spectra (500 MHz, 298 K, CD$_2$Cl$_2$) of a solution of a 1:1 mixture of **8**$^+$ and DB24C8 (3 mM) (black line), the signals associated with the complex are highlighted in red, a solution of **8**$^+$ (3 mM) (blue line) and a solution of DB24C8 (3 mM) (green line).
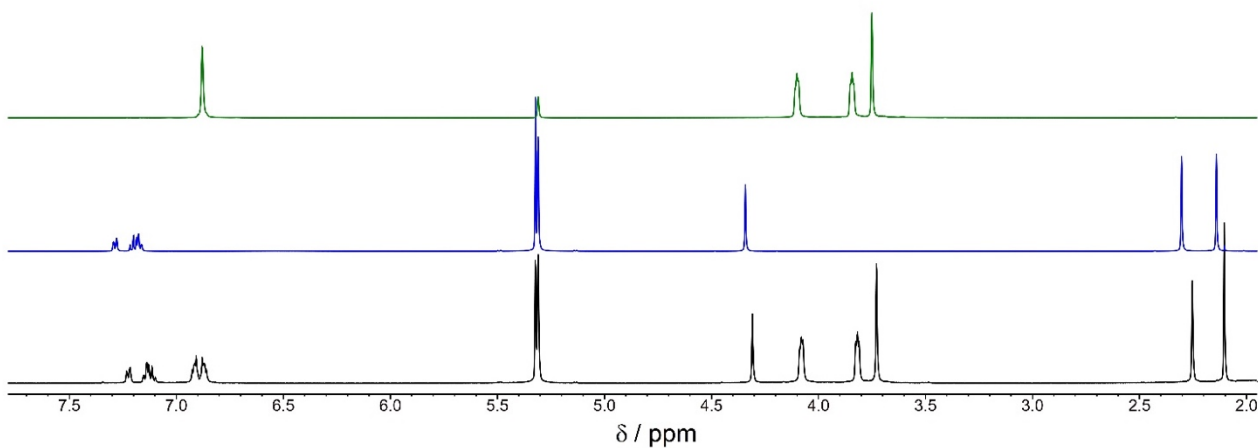
Figure S34. ^{1}H NMR spectra (500 MHz, 298 K, CD$_2$Cl$_2$) of a solution of a 1:1 mixture of **9$^+$** and DB24C8 (3 mM) (black line), the signals associated with the complex are highlighted in red, a solution of **9$^+$** (3 mM) (blue line) and a solution of DB24C8 (3 mM) (green line).
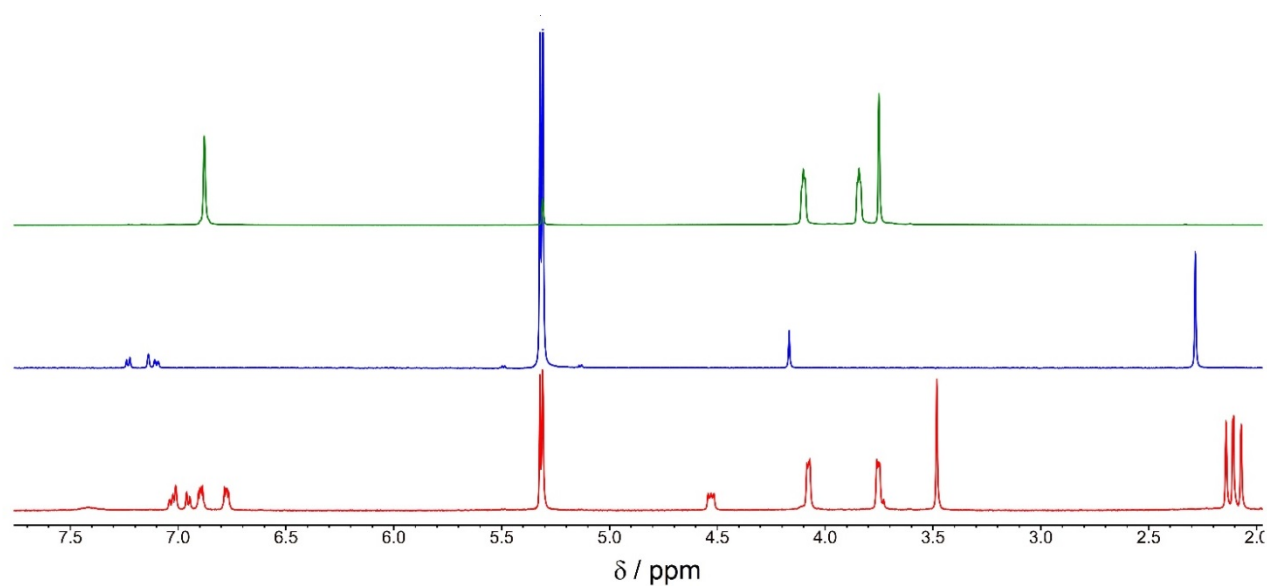

Figure S35. ^{1}H NMR spectra (500 MHz, 298 K, CD$_2$Cl$_2$) of a solution of a 1:1 mixture of **10$^+$** and DB24C8 (3 mM) (black line), the signals associated with the complex are highlighted in red, a solution of **10$^+$** (3 mM) (blue line) and a solution of DB24C8 (3 mM) (green line).
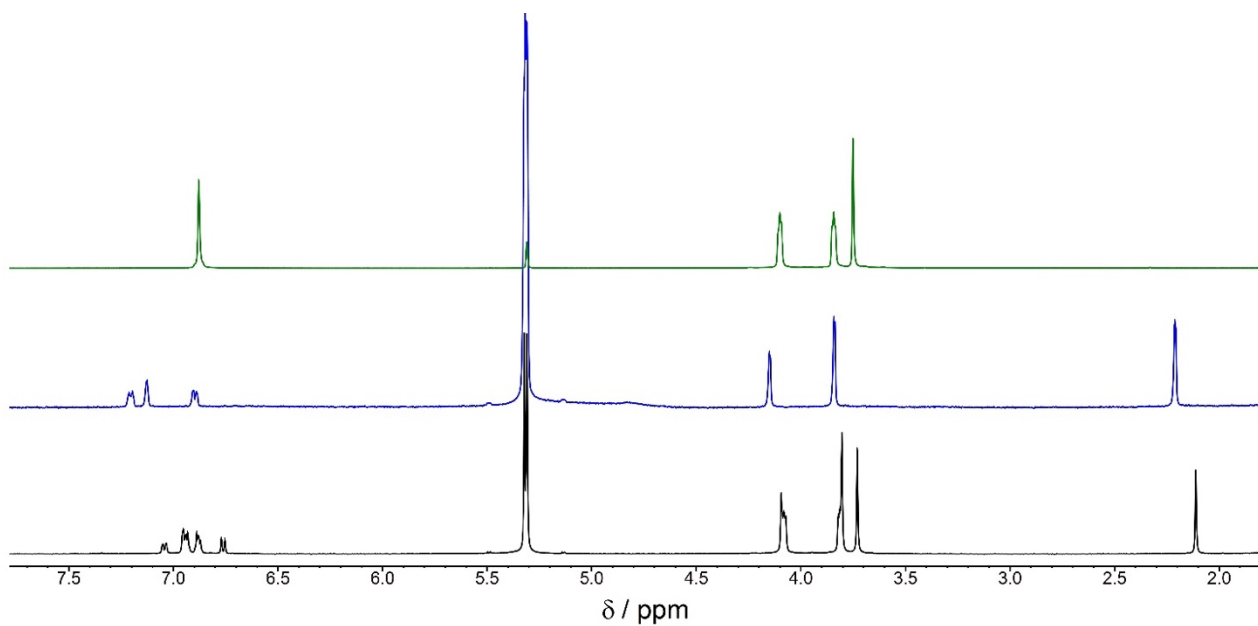
References

[1]   P. R. Ashton, E. J. T. Chrystal, P. T. Glink, S. Menzer, C. Schiavo, N. Spencer, J. F. Stoddart, P. A. Tasker, A. J. P. White, D. J. Williams, *Chem. Eur. J.* **1996**, *2*, 709-728.

[2]   SPECFIT, R. A. Binstead, Spectrum Software Associates, Chapel Hill, NC, **1996**.

[3]   N. Azizi, E. Akbari, A. K. Amiri, M. R. Saidi, *Tetrahedron Lett.* **2008**, *49*, 6682-6684.

[4]   J.-D. Chai, M. Head-Gordon, *Phys. Chem. Chem. Phys.* **2008**, *10*, 6615-6620.

[5]   Gaussian 09, Revision B.01, M. J. Frisch, G. W. Trucks, H. B. Schlegel, G. E. Scuseria, M. A. Robb, J. R. Cheeseman, G. Scalmani, V. Barone, B. Mennucci, G. A. Petersson, H. Nakatsuji, M. Caricato, X. Li, H. P. Hratchian, A. F. Izmaylov, J. Bloino, G. Zheng, J. L. Sonnenberg, M. Hada, M. Ehara, K. Toyota, R. Fukuda, J. Hasegawa, M. Ishida, T. Nakajima, Y. Honda, O. Kitao, H. Nakai, T. Vreven, J. A. Montgomery, Jr., J. E. Peralta, F. Ogliaro, M. Bearpark, J. J. Heyd, E. Brothers, K. N. Kudin, V. N. Staroverov, T. Keith, R. Kobayashi, J. Normand, K. Raghavachari, A. Rendell, J. C. Burant, S. S. Iyengar, J. Tomasi, M. Cossi, N. Rega, J. M. Millam, M. Klene, J. E. Knox, J. B. Cross, V. Bakken, C. Adamo, J. Jaramillo, R. Gomperts, R. E. Stratmann, O. Yazyev, A. J. Austin, R. Cammi, C. Pomelli, J. W. Ochterski, R. L. Martin, K. Morokuma, V. G. Zakrzewski, G. A. Voth, P. Salvador, J. J. Dannenberg, S. Dapprich, A. D. Daniels, O. Farkas, J. B. Foresman, J. V. Ortiz, J. Cioslowski, D. J. Fox, Gaussian, Inc., Wallingford CT, **2010**.

[6]   J. Tomasi, B. Mennucci, R. Cammi, *Chem. Rev.* **2005**, *105*, 2999.

[7]   R. Car, M. Parrinello, *Phys. Rev. Lett.* **1985**, *55*, 2471.

[8]   a) A. Laio, M. Parrinello, *Proc. Natl. Acad. Sci. U.S.A.* **2002**, *20*, 12562-12566; b) M. Iannuzzi, A. Laio, M. Parrinello, *Phys. Rev. Lett.* **2003**, *90*, 238302.

[9]   J. P. Perdew, K. Burke, M. Ernzernhof, *Phys. Rev. Lett.* **1996**, *77*, 3865.

[10] S. Grimme, *J. Comp. Chem.* **2006**, *27*, 1787-1799.

[11] D. Vanderbilt, *Phys Rev. B* **1990**, *41*, 7892.

[12] S. Nosé, *J. Chem. Phys.* **1984**, *81*, 511-519.

[13] W. G. Hoover, *Phys. Rev. A* **1985**, *31*, 1695-1697.

[14] D. Marx, J. Hutter, *Ab Initio Molecular Dynamics*, Cambridge University Press, **2009**.

[15] http://www.cpmd.org. Copyright IBM Corp. 1990-2019, MPI für Festkörperforschung Stuttgart, 1997-2001.

[16] S. R. Billeter, A. Curioni, W. Andreoni, *Comput. Mater. Science*, **2003**, *27*, 437-445.